Stratification and productivity in the Western Tethys (NW Algeria) during early Toarcian.

Hicham Baghli, Emanuela Mattioli, Jorge E. Spangenberg, Wolfgang Ruebsam, Lorenz Schwark, Mustapha Bensalah, Abbès Sebane, Bernard Pittet, Pierre Pellenard, Guillaume Suan

Stratification and productivity in the in the Western Tethys (NW Algeria) during early Toarcian

Hicham Baghli[1,2], Emanuela Mattioli[1,3*], Jorge E. Spangenberg[4], Wolfgang Ruebsam[5], Lorenz Schwark[5,6], Mustapha Bensalah[2], Abbès Sebane[7], Bernard Pittet[1], Pierre Pellenard[8], Guillaume Suan[1]

[1]Univ Lyon, UCBL, ENSL, UJM, CNRS, LGL-TPE, F-69622, Villeurbanne, France
[2]Laboratoire de Recherche n° 25, Université de Tlemcen, Algérie
[3]Institut Universitaire de France (IUF), Paris, France
[4]Institute of Earth Surface Dynamics (IDYST), University of Lausanne, Building Géopolis, CH-1015 Lausanne, Switzerland
[5]Institute of Geosciences, Kiel University, Ludewig-Meyn Str. 10, 24118 Kiel, Germany
[6]Curtin University, WA-OIGC - Department of Earth and Planetary Sciences, 6845 Bentley Campus, Perth, Australia
[7]Laboratoire Géodynamique des Bassins et Bilan sédimentaire (GéoBaBiSé), FSTU, Département de Géologie, Université Oran2 Mohamed BEN-AHMED, Algérie
[8]Biogéosciences, UMR 6282 uB/CNRS, Université Bourgogne Franche-Comté, 6 Boulevard Gabriel, 21000 Dijon

* Corresponding author: Emanuela Mattioli, Univ Lyon, UCBL, ENSL, UJM, CNRS, LGL-TPE, F-69622, Villeurbanne, France and Institut Universitaire de France (IUF), Paris, France

E-mail addresses: baghli.hicham@gmail.com (Hicham Baghli), emanuela.mattioli@univ-lyon1.fr (Emanuela Mattioli), jorge.spangenberg@unil.ch (Jorge E. Spangenberg), wolfgang.ruebsam@googlemail.com (Wolfgang Ruebsam), lorenz.schwark@ifg.uni-kiel.de (Lorenz Schwark), mus.bensalah@yahoo.fr (Mustapha Bensalah), sebane.abbes@yahoo.fr (Abbès Sebane), bernard.pittet@univ-lyon1.fr (Bernard Pittet), Pierre.Pellenard@u-bourgogne.fr (Pierre Pellenard), guillaume.suan@univ-lyon1.fr (Guillaume Suan)

Abstract

Profound environmental changes punctuated the Early Jurassic period, as recorded by marked carbon and oxygen isotope anomalies and major biotic crises. The response of low-latitude regions of Northern Gondwana to such intense changes is not documented as well as that of other Tethys areas. We present new calcareous nannofossil assemblages from three sections located in NW Algeria, in the Sahara and Tlemcen Basins, respectively. New stable carbon and nitrogen isotope data are provided from the Tlemcen Basin to reconstruct local environmental conditions in the wider context of a Toarcian greenhouse climate. We first established a solid chemo- and biostratigraphic framework by integrating stable carbon isotope data and calcareous nannofossil events. Calcareous nannofossil assemblages show common trends in the two basins, such as the occurrence in high proportions of the deep-dweller species *Mitrolithus jansae*, likely indicating stratification of the water column with a deep nutricline. This taxon dominated the assemblage during the negative carbon isotope excursion (CIE) interval, often used to delineate the base of the Toarcian anoxic event (T-OAE). Such a nannofossil record is unique in the Western Tethys domain, as *M. jansae* is known to drastically decrease in abundance during the T-OAE until its disappearance in the aftermath of the event. The NW Algeria nannofossil record indicates prolonged thermal stratification of water-masses, finally triggering hyper-oligotrophy and low productivity in shallow waters during the Toarcian CIE. Such peculiar conditions are likely related to the combined effects of a warm and arid climate dominating along the northern Gondwana margin and the presence of a strong clockwise gyre over the epicontinental shelf, which brought warm equatorial waters from the Tethys Ocean to the NW Algeria shelf.

Keywords: lower Jurassic; Pliensbachian-Toarcian environments; Northern Gondwana; calcareous nannofossils; C and N stable isotopes.

1. Introduction

The Early Jurassic was an upheaval period, characterized by considerable climate and environment changes. These include a drop in seawater temperature in the late Pliensbachian followed by a warming in the early Toarcian (McArthur et al., 2000; Guex et al., 2001; Rosales et al., 2004; Gómez et al., 2008; Suan et al., 2008; 2010; Korte and Hesselbo, 2011; Li et al., 2012; Price et al., 2016; Baghli et al., 2020; Ruebsam et al., 2020c), the development of widespread anoxia/euxinia in epicontinental basins of the northern European epicontinental seaway (Jenkyns, 1988; Prauss et al., 1991; Schwark and Frimmel, 2004; Ruebsam et al., 2018; McArthur, 2019; Remírez and Algeo, 2020a), as well as biological crises and extinctions (Harries and Little, 1999; Wignall, 2001; Macchioni and Cecca, 2002; Gómez et al., 2008; Mattioli et al., 2008; Gómez and Goy, 2011). Major environmental changes coincided with a global disturbance of the carbon cycle as indicated by two negative carbon isotope excursions (CIEs) at the Pliensbachian/Toarcian boundary and during the so-called Jenkyns Event (Toarcian Oceanic Anoxic Event, T-OAE; Jenkyns, 1988; Müller et al., 2017). Negative CIEs were recorded globally in various substrates, including marine carbonates, marine and terrestrial organic matter, and fossil wood, and in different localities around the world (e.g., Jenkyns, 1988; Jenkyns and Clayton, 1997; Hesselbo et al., 2000; Schouten et al., 2000; Kemp et al., 2005; van de Schootbrugge et al., 2005; Suan et al., 2008; Sabatino et al., 2009; McArthur et al., 2008; Wilmsen and Neuweiler, 2008; Littler et al., 2009; Baghli et al., 2020; Remírez and Algeo, 2020b). Numerous studies attempted an improved understanding of the causal links between all the events that occurred during the late Pliensbachian-early Toarcian interval, and at assessing their impact on marine and continental biosphere.

Significant trends in oxygen isotope values of fossilized marine shells attest to major warming phases at the Pliensbachian/Toarcian boundary and in the early Toarcian (Polymorphum-Levisioni zonal transition). As for the CIEs, these temperature fluctuations are recorded in various regions although with different intensities (see Baghli et al., 2020 for a review). Conversely, changes in oxygenation (McArthur, 2019) as well as biotic responses (Mattioli et al., 2008; Rita et al., 2016) seem to have been strongly modulated by regional processes, with marginal basins of the north-eastern Tethys

93 recording prolonged phases of anoxia, whilst southern and western regions of Tethys
94 remained relatively well-oxygenated (Baroni et al., 2018; McArthur, 2019).
95 In this paper, we address the palaeoenvironmental changes that took place in NW
96 Algeria, which was located along the southwestern margin of the Tethys corresponding
97 to the Northern Gondwana shelf. This region shows peculiar features, since it was
98 characterized by arid and warm climate conditions during the Jurassic. Temperatures
99 are assumed to have been 2 to 4°C higher in NW Algeria with respect to other studied
100 areas (e.g., Portugal, Spain, France, England), attesting for a pronounced latitudinal
101 temperature gradient in the western Tethys (Baghli et al., 2020). Carbon isotope values
102 ($\delta^{13}C$) of biogenic calcite (brachiopod shells) show a systematic positive offset of ~0.5‰
103 for values in NW Algeria with respect to the regions cited above (Baghli et al., 2020),
104 suggesting that the C-isotope composition of the Early Jurassic dissolved inorganic
105 carbon (DIC) was spatially heterogeneous in shallow shelf waters of the SW Tethys,
106 possibly linked to regional productivity patterns (e.g., oligo- *vs*. eutrophic regimes,
107 proximal *vs*. distal continental sources, upwelling areas, etc.). The response of primary
108 producers to the environmental perturbations occurring during the late Pliensbachian-
109 early Toarcian interval in northern Gondwana thus needs to be elucidated, especially for
110 those periods recording perturbations of the carbon cycle. Calcareous nannoplankton is
111 an ideal group of microorganisms to address these questions as modern
112 coccolithophorids coevally perform photosynthesis and biocalcification. Their distribution,
113 species richness and abundance are largely controlled by temperature, nutrients, and
114 salinity of surface waters (Winter et al., 1994).
115 Here we present new calcareous nannofossil data, including first (FO) and last
116 occurrences (LO) of species, and assemblage composition based on absolute and
117 relative abundances of three NW Algeria sections (Mellala, Raknet El-Kahla, and Djebel
118 Chemarikh). A biostratigraphic frame based upon calcareous nannofossils is presented
119 for this region for the first time. We present also new stable carbon isotope
120 measurements on whole-rock carbonate and bulk organic samples from the Mellala
121 section. Such analyses on stable carbon isotopes are complemented by measurements
122 of nitrogen stable isotopes and of weight percent total organic carbon (TOC). These
123 measurements, along with previously published geochemical data from the Raknet El-

Kahla section (Reolid et al., 2012b; Ruebsam et al., 2020a), allow a precise bio- and chemo-stratigraphic correlation of the two sections. The changes through time of calcareous nannofossil absolute abundance and assemblage are thus compared with similar records from other basins in order to evaluate local *vs*. regional patterns in the response of marine primary producers to Early Jurassic palaeoenvironmental perturbations.

2. Geological setting

The studied sections are located in two different settings in NW Algeria, which during the Jurassic was located in the NW of Gondwana and corresponded to the southern part of the Western Tethys (Fig. 1). The two regions are nowadays placed on both sides of the Oran High Plains or "Oran Meseta", which is located between the Saharan Atlas to the South and the Tlemcen Domain to the North. From a palaeogeographic point of view, the Oran Meseta comprised a shallow carbonate platform during the Pliensbachian, while a partly emerged and restricted sabkha developed during the Toarcian (Elmi and Alméras, 1984). These areas extended to the West into the Moroccan High Plateaus.

One of the regions studied is located in the Tlemcen Domain, which was a shallow-sea carbonate platform during the late Sinemurian-early Pliensbachian interval. The platform was partly flooded during the early Pliensbachian. Eventually, the Tlemcen Domain differentiated into an intra-cratonic basin divided into wider or narrower sub-basins separated by persistent shoals, which were alternatively flooded or emerged according to sea-level changes (Elmi and Alméras, 1984). The selected section in the Tlemcen domain is Mellala (35°3'54''N, 1°45'39''W; Traras Mountains, Beni Menir sector). The Traras Mountains are bounded to the North by the Mediterranean Sea, to the East by the Mio-Plio-Quaternary Tafna Basin, to the West by the Beni Snassen Mountains (Eastern Middle Atlas in Morocco), and to the South by the Maghnia Trough (geologic map of Algeria 1/500.000; 2nd Edition, 1952). This section was selected because of the good exposure of a thick and continuous sedimentary succession of the Pliensbachian/Toarcian transition, with a monotonous succession of alternating marls

and marly limestones (Ameur, 1999; Elmi et al. 2006). At Mellala, the exposed succession includes the Pliensbachian/Toarcian boundary up to the Toarcian Bayada Formation, which is represented by hemipelagic facies. The common occurrence of ammonites, brachiopods and foraminifera provides a precise biostratigraphic frame enabling the recognition of the Emaciatum Ammonite Zone (Elisa Subzone), the Polymorphum Ammonite Zone (Mirabile and Semicelatum subzones) and the Levisoni Ammonite Zone (Elmi et al., 2006; Reolid et al., 2014a).

The second region of study is located in the Atlas system, which represents the southern palaeo-margin of the western Tethys and possesses a geometry directly inherited from the Early Mesozoic rifting of both the Central Atlantic and the Alpine Tethys domains (Aït Ouali, 1991; Favre, et al., 1991). The successions studied belong to the Sahara Atlas, which is a slightly deformed Meso-Cenozoic intracontinental mountain chain (Frizon de Lamotte et al., 2009), extending from the Moroccan Middle and High Atlas to the West, and passing into the Tunisian Trough to the East. This region was bounded in Algeria by the Oran Meseta to the North, and by the Sahara platform to the South. The Sahara Atlas can be subdivided into three sub-domains: the Ksour Mountains (Western Sahara Atlas), the Djebel Amour (Central Sahara Atlas), and the Ouled Naïl, Aurès, Hodna and Nememcha-Mzab Mountains (Eastern Sahara Atlas) (Ritter, 1902; Bracène and Frizon de Lamotte, 2002).

Our study is focused on the Pliensbachian-Toarcian sections located in the Western Sahara Atlas (Ksour Mountain). The core of this inverted-rift structure belt consists of a Palaeozoic metamorphic basement. The overlying sedimentary cover comprises marine and continental deposits of Mesozoic and Cenozoic age. The most prominent feature of the Atlas domain (Ksour Mountains) compared to the Tlemcen domain is the early development of a carbonate platform, probably as early as the Rhaetian-Hettangian in the Aïn Ouarka area (Sahara Basin; Elmi et al., 1998), the most rapidly subsiding sub-basin of the Saharian Atlas.

We studied two sections, Djebel Chémarikh (32°41’30"N, 0°10’26’’W) and Raknet El-Kahla (32°44’17’’N, 0°7’37’’W), which are located in the Aïn Ouarka sector. This area presents four formations, namely: (i) the Chemarikh dolomite Formation (Hettangian) corresponding to an inner platform sedimentary environment; (ii) the marl-limestone

alternations of Aïn Ouarka Formation (Sinemurian to Pliensbachian in age), showing the evolution from an external platform, a sedimentary ramp, to a deep basin; (iii) the rhythmic marl-limestones of the Aïn Rhézala Formation (Toarcian to Aalenian in age), which are interpreted as having been deposited in the Atlas depocentre; and, finally, (iv) the Raknet El-Kahla conglomerates (Aalenian to Bajocian in age; Mekahli, 1998; Mekahli et al., 2004). We focused on the part of the Raknet El-Kahla section covering the Emaciatum Zone (late Pliensbachian) to the Levisoni Zone (early Toarcian), and on the Djebel Chemarikh section covering the interval from the middle Toarcian (Bifrons Zone) to the late Toarcian (Aalensis Zone).

3. Material and methods

3.1. Carbon isotope composition of carbonates

Sixty-one bulk rock samples from the Mellala section (latitude and longitude: 35°3'54''N, 1°45'39''W; along the road RN98 between Tlemcen and Ghazaouet, just at the intersection with the road RN99A to Nedroma, height comprised between 130 and 150 m), ranging in age from the late Pliensbachian to the middle Toarcian, were analysed for their carbon isotope composition ($\delta^{13}C_{carb}$). The carbon isotope measurements on bulk rock were performed using a Thermo Fisher Scientific (Bremen, Germany) Gas Bench II and carbonate preparation device, connected to a Delta Plus XL isotope ratio mass spectrometer at the Institute of Earth Surface Dynamics of the University of Lausanne. The CO_2 extraction was done by reaction of 100–200 µg of powdered carbonate sample with anhydrous phosphoric acid at 70°C. The carbon isotope ratios ($R = {}^{13}C/{}^{12}C$) are reported in the delta (δ) notation as the per mil (‰) deviation relative to the Vienna Pee Dee belemnite standard (VPDB): δ_{sample} (‰) = [($R_{sample} - R_{standard}$) / $R_{standard} - 1$] × 1000. The standardization of the $\delta^{13}C$ values relative to VPDB was done by replicate analysis of the in-house working standard Carrara marble (UNIL-CM, $\delta^{13}C$ = 1.95 ‰) within the analytical sequences. The $\delta^{13}C$ values of the reference CO_2 gas and the UNIL-CM standard were obtained by normalization with the international reference materials NBS-19 limestone ($\delta^{13}C$ = +1.95 ‰), NBS-18 carbonatite ($\delta^{13}C$ = –5.01 ± 0.03 ‰), and LSVEC lithium carbonate ($\delta^{13}C$ = –46.6 ‰). The used $\delta^{13}C$ values were those

recommended by Brand et al. (2014). Analytical uncertainty (1σ), monitored by replicate analyses of NBS-19 and UNIL-CM was not greater than ±0.05 ‰ for $\delta^{13}C$.

3.2. Organic carbon isotopes and TOC

The same samples from Mellala analysed for whole-rock carbon stable isotopes were also analysed for TOC content and for bulk organic carbon isotopes ($\delta^{13}C_{org}$) at the Institute of Geosciences, Kiel University. The TOC content was determined on decalcified samples. Decalcification was achieved by treating samples with HCl (10% and 25%) to remove calcium carbonate and dolomite. Subsequently, the samples were washed and neutralized with deionized water and dried in an oven at 40°C for 48 hours. Values determined on decalcified samples were corrected for their carbonate loss to yield original TOC concentrations. Reproducibility and accuracy were checked by running replicate analysis of laboratory standards and duplicate analysis of samples and were better than 0.1 wt.% (1σ).

Stable carbon isotope analysis of the bulk organic carbon ($\delta^{13}C_{org}$ values) were performed on decalcified samples using a Thermo Scientific Delta V isotope ratio mass spectrometer coupled to a Flash EA via a Conflow III interface. The measured $\delta^{13}C$ values were calibrated to the VPDB scale with the international reference material caffeine standard (IAEA-600, $\delta^{13}C$ = –27.77‰ ~~VPDB~~). Reproducibility and accuracy were monitored by replicate standard and sample analysis and were better than 0.1‰ (1σ).

3.3. Nitrogen isotopes

Nitrogen stable isotope analysis of the bulk sediment ($\delta^{15}N_{tot}$) was performed on the original sample material in order to avoid decalcification-induced alteration of the isotopic signature (Vafeiadou et al., 2013; Schlachter and Connolly, 2014; Ruebsam et al., 2020a). $\delta^{15}N_{tot}$ measurements were performed using a Thermo Scientific Delta V isotope ratio mass spectrometer coupled to a Flash EA via a Conflow III interface. The Flash EA was equipped with a large volume reactor, allowing analysis of samples low in

249 total nitrogen abundances. The nitrogen isotope ratios ($^{15}N/^{14}N$) are expressed in the
250 delta notation, as ‰ deviation relative to the nitrogen in air (Air-N_2) standard.
251 Reproducibility and accuracy were monitored by replicate standard and sample analysis
252 and were better than 0.1‰ for standard materials and 0.3‰ for samples (1σ). The
253 measured $\delta^{15}N$ values were calibrated the IAEA-600 caffeine standard ($\delta^{15}N$ = +0.91‰).
254
255 *3.4. Calcareous nannofossils*
256
257 A total of 117 samples were analysed for calcareous nannofossils analysis
258 including: 34 samples from the Mellala section, spanning from the upper Pliensbachian
259 to the lower Toarcian (Fig. 2; Table 1), 34 samples from Raknet El-Kahla section,
260 covering the upper Pliensbachian to the middle Toarcian (Fig. 2; Table 2), and 59
261 samples from Djebel-Chemarikh section, spanning the middle to upper Toarcian (Fig. 2;
262 Table 3). Slides for calcareous nannofossil analyses were prepared according to the
263 settling technique described by Beaufort et al. (2014) slightly modified. A small amount
264 of sediment powder was mixed in a tube with a known volume of water. After stirring, the
265 tube was placed in an ultrasonic bath for few seconds to separate sediments and
266 coccoliths, and the obtained suspension of water and sediment powder was poured onto
267 a precisely weighted coverslip placed in a Petri dish. After settling for 4 hours, the water
268 was carefully removed using a water-pump and the slide was dried in an oven to remove
269 residual water. Once the slide dried, the coverslip was weighted a second time to
270 calculate the amount of powder homogeneously settled on the slide. Finally, the
271 coverslip was mounted onto a microscope slide using Rhodopass B resin (polyvinyl
272 acetate). The obtained slides were observed in a ZEISS Axioscope 40 polarising
273 microscope, using a 1000X magnification. A minimum of 300 specimens per samples
274 were counted in a variable area of the slide, and fifty fields of view were further scanned
275 for each slide in order to identify rare species. The counting of 300 specimens is
276 statistically significant to record all the species making up more than 1.7% of total
277 assemblage with 99.5% confidence level (Fatela and Taborda, 2002).
278 An assessment of the degree of preservation was made for each sample, based on
279 the degree of etching and overgrowth, as reported by Roth (1984). Three classes of

preservation were thus used: poor for nannofossil assemblages showing strong etching, overgrowth or fragmentation, moderate and good when *Schizosphaerella* fragmentation is limited and delicate coccoliths showing relatively pristine structures were found, respectively. For the Mellala and Raknet El-Kahla sections, we also calculated the absolute abundance of calcareous nannofossils per gram of rock using the following formula:

$$X = n \times A^t \times m^{-1} \times A^{-1} \quad (1)$$

where X is the absolute abundance, n is the number of counted specimens in a slide, A^t is the total area of the cover slide, m is the mass of the weighted rock powder and A is the area studied in the slide.

In Raknet El-Kahla, the volume of *Mitrolithus jansae* was also estimated on 30 specimens per sample in 14 samples (except in sample RK01, where well preserved specimens were very rare). For each of the 14 samples, the image from the first 30 specimens randomly recorded was captured with a Leica EC3 digital camera, coupled with an optical polarized light microscope (X1000 magnification). In the system we used, 1 µm correspond to 17.5 pixels, thus the precision of size measurements is 0.057 µm per pixel. For each coccolith, 4 parameters (H: height of the coccolith with the spine; h: height of the coccolith; R: diameter at the top of the coccolith; r: diameter at the base of the coccolith) were measured using the software ImageJ©. The volume of the coccoliths was thus estimated on the basis of the formula defined by Suan et al. (2008):

$$V = 1/3 \times \pi \times (H \times h/2) \times (R^2 + R \times r + r^2) \quad (2)$$

Measurements of the coccolith parameters were used to calculate simple statistical parameters, such as mean and standard deviation. Statistical analysis was performed using the PAST 3.01 software package (Hammer et al., 2001).

4. Results

311 *4.1. Stable isotope data and wt.%TOC*

312

313 The new $\delta^{13}C_{carb}$ and $\delta^{13}C_{org}$ data obtained for Mellala were compared to the
314 published data for Raknet El-Kahla (Reolid et al., 2012b; Ruebsam et al., 2020a). The
315 long-term trends and magnitude of changes in $\delta^{13}C_{carb}$ values are similar in the two
316 sections (Fig. 2). The $\delta^{13}C_{carb}$ values oscillate around 0‰ in the late Pliensbachian,
317 decrease at the Pliensbachian/Toarcian boundary (Pl/To CIE) and reach minimum
318 values of about –3.0‰ (–3.1‰ in Raknet El-Kahla, and –2.9‰ in Mellala) at the base of
319 Polymorphum Zone, then record a positive rebound to approximately +0.8‰ (0.8‰ in
320 Raknet El-Kahla, and 0.7‰ in Mellala) in the middle-upper part of the Polymorphum
321 Zone. The $\delta^{13}C_{carb}$ values decrease again in the basal part of the Levisoni Zone in both
322 sections (down to –1.3‰ in Raknet El-Kahla, and –2.3‰ in Mellala), thus capturing
323 partially or totally the CIE often associated with the T-OAE.

324 The $\delta^{13}C_{org}$ values measured in Mellala vary from –22.0‰ to –29.4‰. The $\delta^{13}C_{org}$
325 curve mimics the general trends of the $\delta^{13}C_{carb}$ curve. Two relative minimum $\delta^{13}C_{org}$
326 values, namely in the lower part of the Toarcian and across the Polymorphum/Levisoni
327 zones boundary (NJT6a nannofossil zone), interrupt a general increasing trend of
328 $\delta^{13}C_{org}$ values across the lower Toarcian (dark grey shaded areas in Fig. 2).

329 The $\delta^{15}N$ values range from 0.3‰ to 3.9‰. The highest values are recorded in the
330 uppermost Pliensbachian, where the $\delta^{15}N$ curve greatly fluctuates from values at around
331 1‰ to values at around 4‰. In the Mirabile Subzone of earliest Toarcian, values
332 decrease to 1-2‰ and, in the Semicelatum Subzone, $\delta^{15}N$ values attain up to 3‰ in
333 discrete levels. Some of the lowest values are recorded in the Levisoni Zone, in the
334 ointerval corresponding to the T-OAE interval (Fig. 2).

335 The TOC contents are overall very low and do not exceed 0.45%, with the lowest
336 values restricted to intervals corresponding to the two negative CIEs at the base of the
337 Toarcian, the Mirabile Subzone, and in the Levisoni Zone (Fig. 2).

338

339 *4.2. Calcareous nannofossils record*

340

341 *4.2.1. Calcareous nannofossils bio-events*

Preservation state is poor to moderate in most of the analysed samples of the three studied sections (Tables 1-3; Plates 1-2). The poor calcareous nannofossil preservation is coherent with clay mineralogy data, wich indicate a strong burial diagenesis similar to sites in the High-Altas of Morocco (Supplementary Material). However, preservation state did not prevent the species identification or the counting of 300 specimens per slide. Thus, it was considered sufficient to evaluate primary changes in calcareous nannofossil assemblages related to environmental fluctuations.

The biostratigraphic scheme used here follows that of Mattioli and Erba (1999), defining the nannofossil zones and subzones for the Mediterranean Tethys, eventually implemented by Ferreira et al. (2019). The ammonite zonation of Raknet El-Kahla and Djebel Chémarikh sections have been previously defined by Mekahli (1998), and that of Mellala is after Elmi et al. (2006). Several nannofossil bio-events were recorded in the Raknet El-Kahla section, from the Emaciatum Zone (late Pliensbachian) to the Bifrons Zone (middle Toarcian) and in the Djebel Chemarikh section, from the middle to the late Toarcian (Fig. 2). A series of successive events characterizes the Pliensbachian/Toarcian boundary in Raknet El-Kahla or Mellala, namely the FOs of *Crepidolithus impontus*, *Diductius constans*, *Biscutum dubium*. Other events are recorded across the boundary, such as the FO of *Biscutum intermedium*, which is observed in both sections very close to the Pliensbachian/Toarcian boundary. The FO of *Discorhabdus ignotus* in the lowermost part of the Polymorphum Zone coincides in both sections with the Pl/To CIE (Fig. 2; Tables 1 and 2). This species is temporarily absent in the samples coinciding with the CIE of the early Toarcian (T-OAE equivalent interval) in Raknet-El-Khala section (Fig. 2; Table 2).

The FO of *Carinolithus superbus* (*C. superbus crassus* of Visentin et al., 2020), which is the marker of the NJT6 nannofossil zone, was identified in the Raknet El-Kahla and Mellala sections in the Polymorphum ammonite Zone, concomitant with the positive rebound of the carbon isotope curve. The NJT6 zone includes the CIE often used to define the base of the T-OAE (Fig. 2). In several sections of the Tethys domain, this zone is subdivided into a and b according to the LO of *Mitrolithus jansae* (Ferreira et al.,

2019). This is not possible in the Raknet El-Khala section because the LO of *M. jansae* is recorded after the FO of *D. striatus*.

The FO of *Discorhabdus striatus* is recorded in the interval just above the T-OAE negative CIE in Raknet El-Kahla (Fig. 2). This event marks the base of the NJT7 zone. This event is closely followed by the FO of *Watznaueria colacicchii* in the Levisoni Zone and by the LO of *Mitrolithus jansae* in the upper part of Levisoni Zone. In the Bifrons Zone of Raknet El-Kahla, thin and elongated specimens of *Carinolithus superbus* first occur (*C. superbus superbus* of Visentin et al., 2020).

In Djebel Chemarikh section, the presence of *Watznaueria fossacincta* was identified in sample at the base of the Bifrons Zone (Sublevisoni Subzone). The FOs of *Triscutum sullivanii* and of *Biscutum depravatum* followed by the FO of *Discorhabdus criotus* in the also occur in the Bifrons Zone (Fig. 2; Table 3). Finally, the FO of *Watznaueria contracta* characterizes the top of the late Toarcian Meneghinii Zone, and the FO of *Hexalithus magharensis* the base of the Aalenian (Fig. 2; Table 3).

4.2.2. Nannofossils absolute abundances

Absolute and relative abundances were calculated for samples ranging from the upper Pliensbachian to the middle Toarcian, of the Raknet El-Kahla and Mellala sections. Nannofossils were deemed too scarce in the Djebel Chémarikh section (middle to upper Toarcian) to estimate their absolute abundance per gram of rock. This scarcity is partly attributable to a poor preservation but possibly also to an originally very low calcareous phytoplankton primary productivity.

The highest nannofossil absolute abundance values in the Raknet El-Kahla section are recorded in the Emaciatum Zone, with values up to $120x10^6$ nannofossils per gram of rock. Then values show a decreasing trend across the Pliensbachian/Toarcian boundary, except for ~~unless~~ a positive peak of $100x10^6$ at the boundary. The absolute abundance values show an average of $40x10^6$during the Polymorphum Zone, with minimum values being attained in Levisoni Zone, corresponding to the T-OAE interval (Fig. 3).

In the Mellala section, absolute abundance shows values higher than at Raknet El-Khala. Average values are around $350x10^6$ in the Polymorphum Zone, although regularly fluctuating between ~150 and $600x10^6$. Such fluctuations are related to the lithology. In fact, values are lower in limestone beds and more important in marls. ~~before~~ Absolute abundance values show a drastic drop down to around $80x10^6$ between the top of the Polymorphum Zone and the base of the Levisoni Zone (Fig. 4).

4.2.3. Trends in calcareous nannofossils assemblages

In both sections (Raknet El-Kahla and Mellala), the relative abundance of *M. jansae* (which is a murolith-coccolith; Bown, 1987) is quite high compared to other species (Figs. 4 and 5). In the Raknet El-Kahla section the relative abundance of *M. jansae* in the late Pliensbachian up to the Levisoni Zone fluctuate between 30% and 70% of total coccoliths (Fig. 3). Despite low total nannofossil absolute abundances, the relative abundance of *M. jansae* stays high during the T-OAE interval. A drastic decrease to values lower than 10% is observed in the upper part of the Levisoni Zone, forewarning the disappearance of this taxon at the base of the Bifrons Zone.

In the Mellala section, the dominance of *M. jansae* over coccoliths is not as important as in Raknet El-Kahla section, high relative abundances are recorded across the Emaciatum and Polymorphum Zones (~40%), then they fall down to ~5% in the upper part of the Mirabile Subzone. *Mitrolithus jansae* relative abundances increased again to about 20% in the Semicelatum Subzone, and remained high (>20%) in the basal Levisoni Zone, in which nannofossils absolute abundances decreased markedly (Fig. 4).

In the two sections studied, *C. crassus* dominated within the *Crepidolithus* pool. It is more abundant in Raknet El-Kahla (average 12%) than in Mellala (average 6%). The relative abundances of *Crepidolithus* spp. increased only in the Levisoni Zone, above the CIE interval, when the *M. jansae* relative abundances decreased.

Within the placolith-coccolith group (definition in Bown, 1987), the relative abundances of *Lotharingius* spp. display in both sections an increase after the Pliensbachian/Toarcian boundary and stay high in the Polymorphum and Levisoni Zones.

The Biscutaceae show high percentages in both sections, especially in the Polymorphum Zone of the Mellala section, where their relative abundances exceed those of *M. jansae*. However, an opposite trend in relative abundances of these two taxa is observed (Fig. 4).

Absolute and relative abundances of the *incertae sedis Schizospharaella* spp. display a peculiar pattern (Figs. 4 and 5), with relatively high abundances although fluctuating in the late Pliensbachian and early Toarcian. A clear decrease is observed across the Pliensbachian/Toarcian boundary in the Mellala section, passing from abundances >25% below the boundary to ~10% above the boundary. A similar trend is observed in Raknet El-Kahla section, with abundances >20% below, and <10% above the Pliensbachian/Toarcian boundary. However, the most relevant decrease in the taxon abundance is observed at the base of the T-OAE CIE, with values <5% of the total nannofossil assemblage in both sections.

The measurements of *M. jansae* in the Raknet El-Kahla section (Fig. 3) show an average volume of 85.67 μm^3 and no significant stratigraphic changes. In particular, *M. jansae* volumes remained relatively constant across the two CIEs at the Pliensbachian/Toarcian boundary and the T-OAE (Fig. 3).

5. Discussion

5.1. Ecology of nannofossil taxa

Before discussing the nannofossil trends in the studied sections, a brief review on the ecological preference of main taxa is presented here. Lower Jurassic nannofossils are composed of coccoliths and *Schizosphaerella* (*incertae sedis*). This latter taxon has been long considered as affiliated to dinoflagellate cysts (Bown, 1987). Recently, unicellular planktonic algae of the genus *Phacotus* (Chlorophyta) were reported from lakes of the temperate zone (Szelag-Wasielewska et al., 2018), which are composed of two calcite valves very much resembling the shape of Jurassic *Schizosphaerella* (Menini et al., 2021). Claps et al. (1995) and Tremolada et al. (2005) interpreted *Schizosphaerella* as a deep-dweller taxon, in a way similar to the modern

coccolithophorid *Florisphaera profunda* (Molfino and McIntyre, 1990). A deep-dweller habitat for *Schizosphaerella* was, however, challenged because this taxon was dominating in both proximal, shallow areas and in deeper, and distal settings (Mattioli and Pittet, 2004; Reggiani et al., 2010). *Schizosphaerella* is dominant over coccoliths along the southern Tethyan margin (Bown, 1987; Mattioli et al., 2008), conversely it was recorded as rare in the NW European shelf (Bucefalo Palliani et al., 2002; Mattioli et al., 2008). *Schizosphaerella* might have proliferated in overall oligotrophic waters in times of nutriment recycling in surface waters because of intensified storms (Mattioli, 1997; Mattioli and Pittet, 2004).

Mitrolithus jansae, which is conspicuously recorded in NW Algeria, likely had a deep (or intermediate) dweller ecology (Bucefalo Palliani and Mattioli, 1998; Erba, 2004; Mattioli and Pittet, 2004), and dominated over other coccoliths in times of stratification of the water column when the nutricline settled deep in the photic zone. A possible modern analogous is the deep-dweller species *Florisphaera profunda*, which is dominating the assemblages when surface waters are oligotrophic and the nutricline settles deep (Molfino and McIntyre, 1990). *Mitrolithus jansae* is a typical component of southern Tethyan settings and is rare in the sections located along the northern margin of Tethys (Bown, 1987; Mattioli et al., 2008). A similar deep-dweller habitat has been proposed for the species *Crepidolithus crassus* (Bour et al., 2007; Mattioli et al., 2008; Reggiani et al., 2010; Fraguas, 2014), but this taxon was more widespread along the N-Tethyan margin (Mattioli et al., 2008).

The small placolith-coccoliths belonging to *Lotharingius* and to Biscutaceae may indicate moderate-to-high nutrient concentrations in the shallow photic-zone waters (Pittet and Mattioli, 2002; Mattioli and Pittet, 2004; Olivier et al., 2004; Tremolada et al., 2005). *Lotharingius* and Biscutaceae are very tiny, small coccoliths. In modern oceans, similar coccolith morphology is typical of meso-eutrophic species, which are common in the surface oceanic waters or proximal settings (Young, 1994).

5.2. Biostratigraphy and chemostratigraphy

5.2.1. Nannofossil biozonation and correlation of the studied sections

The recent work of Ferreira et al. (2019), who updated the calcareous nannofossil biostratigraphy of the Lower and Middle Jurassic strata exposed in Portugal, was applied in this study because the locations were situated in a similar paleogeographic and paleoclimatic realm. The nannofossils zones and subzones that have been recognized in Mellala section range from NJT5b to NJT6a, in Raknet El-Kahla range from NJT5b to NJT7b, whereas in Djebel Chemarikh from NJT7a to NJT8f (Fig. 2). The base of the Mellala and Raknet El-Kahla sections is attributed to the nannofossil subzones NJT5b and c, spanning the latest Pliensbachian to earliest Toarcian, because of the consistent presence of *Lotharingius crucicentralis* in the stratigraphically lowermost samples. The species *Zeugrhabdothus erectus*, which defines the boundary between the two subzones NJT5b and c, roughly corresponding to the Pliensbachian/Toarcian boundary, was not recorded in NW Algeria. However, the studied sites record other auxiliary events characterizing the Pliensbachian/Toarcian boundary in several Tethys regions (Fig. 2; Menini et al., 2019).

The base of the NJT6 zone is defined by the FO of *Carinolithus superbus*, and its top is defined by the FO of *Discorhabdus striatus*. According to Ferreira et al. (2019), the NJT6 is subdivided into two subzones, NJT6a and b, on the basis of the LO of *M. jansae*. However, in NW Algeria *M. jansae* last occurs above the FO of *D. striatus*, i.e. in a reverse order compared to most Tethys records, likely because this species survived longer in South Tethys refuge areas. The lower boundary of the nannofossils zone NJT7 is characterized by the FO of *Discorhabdus striatus* in Raknet El-Khala, but the upper boundary is not defined since we did not record the FO of *Retecapsa incompta* in Djebel Chemarikh. In both Raknet El-Kahla and Djebel Chemarikh sections, two subzones can be identified, namely the NJT7a ranging between the FO of *D. striatus* and the FO *Watznaueria colacicchii*, and the NJT7b whose top is defined by the FO of *Discorhabdus criotus* (Fig. 2). These two subzones are not clearly differentiated because the NJT7a corresponds to a very reduced thickness in both sections (Fig. 2a). In Djebel Chemarikh section, two other nannofossil subzones are recognized, namely the NJT7c which ranges between the FO of *D. criotus* and the *Lotharingius* size shift; then after an interval ~20m thick which is not dated by nannofossils, the FO of *Watznaueria contracta*

allowed us to define the base of the NJT8d subzone. Finally, the base of the NJT8f is characterized by the FO of *Carinolithus magharensis* at the top of Djebel Chemarikh section, also marking the base of the Aalenian.

When comparing the nannofossil record and the $\delta^{13}C$ negative excursion of both whole rock carbonate and TOC at the Pl/To boundary in Mellala, it appears that some events (mainly FOs) are stratigraphically separated, whilst in many other Tethys sections including the GSSP in Peniche they occurred very close to each other (Menini et al., 2019). This pattern can be explained by the exceptional continuity of the sedimentary record and higher accumulation rates across the Pl/To boundary in the Mellala section. In fact, this section was originally considered as a potential GSSP candidate for the Pliensbachian/Toarcian, due the remarkable continuity of the sedimentary record and the well-established ammonite biozonation (Elmi et al., 2006). This continuity is relevant because, in many other Tethys settings, sedimentary condensation and hiatuses occur in the same interval (Pittet et al., 2014; Bougeault et al., 2017; Menini et al., 2019; Ruebsam and Al-Husseini, 2020). This sedimentary continuity likely resulted from the tectonic context of the Mellala area, which was defined as a subsiding "umbilicus" (Elmi et al., 2006).

5.2.2. The record in NW Algeria of carbon cycle perturbations based on trends in $\delta^{13}C_{carb}$, $\delta^{13}C_{org}$ and TOC values

The $\delta^{13}C_{carb}$ and $\delta^{13}C_{org}$ profiles in the Mellala section record two CIEs, which occurred at the Pliensbachian/Toarcian boundary (Pl/To CIE) and in the early Toarcian (T-OAE CIE). Trends in inorganic and organic carbon isotopes can be correlated with coeval sites and reflect times of profound carbon cycle perturbations. Both negative CIEs, recognized in various oceanic and continental settings, likely resulted from massive injections of ^{13}C-depleted carbon into the ocean and atmosphere reservoirs (e.g., Hesselbo et al., 2000; 2007; Ruebsam et al., 2020b). Our new data from the Mellala site record the onset of the prominent T-OAE CIE, thus showing many similarities with the $\delta^{13}C_{carb}$ and the $\delta^{13}C_{org}$ data previously obtained for the Raknet El-Kahla section (Reolid et al. 2012b; Ruebsam et al. 2020a) (Fig. 2). This was expected,

given the geographical proximity between the two sites. Recently, the Pl/To CIE has also been recorded in brachiopod calcite from NW Algeria (Baghli et al., 2020).

Following this marked carbon isotope event, a prominent positive $\delta^{13}C_{carb}$ and $\delta^{13}C_{org}$ rebound is recorded in the Polymorphum Zone (early Toarcian) of both Mellala and Raknet El-Khala. This event, also recorded in several Tethys sites, has been attributed to increased sequestration of atmospheric carbon, possibly through reduced carbon emission rates or higher primary production in shallow marine waters (Hesselbo et al., 2007). The bio- and chemostratigraphic data allowed a correlation of the proximal Mellala and the Raknet El-Kahla sections.

The organic carbon content at Mellala (less than 0.5 wt.% TOC) is overall very low, especially if compared to NW Europe sites, where values can attain up to 16 wt.% TOC (e.g., Hesselbo, 2000; Röhl et al., 2001; Hermoso et al., 2013; Suan et al., 2015; Ruebsam et al., 2018). The lowest TOC values are bound to the two negative CIEs at the Pl/To and T-OAE equivalent intervals. Although TOC contents are overall very low (in the range of 0.2 to 0.3 wt.%) also in Raknet El-Kahla, a moderate increase in TOC up to ~0.6% occurs in the T-OAE CIE interval of this latter section and has been attributed to the development of oxygen-deficient bottom and pore waters (Ruebsam et al., 2020a). In this view, although TOC values are very low in both sections, the record of Mellala differs from the one reported from Raknet El-Khala. One explanation might be that oxygen-deficient conditions did not develop at Mellala in the interval of the T-OAE CIE, potentially due to the proximity to the open-shelf sea and less hydrological restriction (Fig. 1). Alternatively, low TOC values during the T-OAE CIE at Mellala may be related to a decreased primary productivity in surface waters. In fact, nannofossil absolute abundances are the lowest in this interval, the meso-eutrophic forms (such as Biscutaceae) are rare, while the deep-dwellers (such as *M. jansae*) indicating marine-water stratification and oligotrophy in the upper photic-zone layer (Bucefalo Palliani and Mattioli, 1998; Mattioli and Pittet, 2004; Erba, 2004; Mattioli et al., 2008) dominate (Fig. 2).

5.2.3. Nutricline fluctuations based on trends of $\delta^{15}N$

588 The $\delta^{15}N$ values measured at Mellala were compared to data acquired in Raknet
589 El-Khala (Ruebsam et al., 2020a). Overall, values are comprised between 0 and 4 ‰ in
590 Mellala, and between 2 and 4 ‰ at Raknet El-Khala. Some of the lowest and steadiest
591 values were recorded in both sections in the intervals corresponding to the two negative
592 CIEs in the Pl/To and T-OAE intervals. More fluctuating values are observed in the
593 Pliensbachian of Mellala and in the upper part of Polymorphum of both sections.
594 Nitrogen fixing diazotroph cyanobacteria add nitrogen to the surface ocean with a
595 fractionation of –3‰ to –1 relative to the atmospheric N_2 source ($\delta^{15}N_{air}$ ~0‰) (Brandes
596 and Devol, 2002; Gruber, 2008). The present-day oceanic value of organic matter $\delta^{15}N$
597 formed from nitrate assimilation is mostly determined by the $\delta^{15}N$ of nitrate delivered to
598 the euphotic zone (the subsurface source), which in turn is dependent on the degree of
599 water column denitrification, and on the degree of nitrate consumption at the ocean
600 surface. Accordingly, changes in organic matter $\delta^{15}N$ can reflect the variability of the
601 source nitrate $\delta^{15}N$ and of the degree of nitrate consumption, but will also vary as
602 function of redox-controlled denitrification rates (e.g., Gruber, 2008; Casciotti, 2016).
603 Throughout the Mellala section, significant changes in the redox conditions are not
604 apparent from sedimentogical observations. Thus, the $\delta^{15}N$ values most likely vary in
605 response to changes in N-uptake (related to primary productivity changes) and in
606 vertical shifts of the nutricline. A reduced N-uptake because of reduced primary
607 productivity drives a decline in $\delta^{15}N$ (Casciotti, 2016; Schoepfer et al., 2016). A shallow
608 nutricline (mesotrophic surface waters) can be linked to nitrate introduced into the water
609 column. This process results in lower $\delta^{15}N$ values. A deep nutricline (oligotrophic surface
610 waters) can be linked to organic matter formed from nitrate assimilation in regions where
611 plankton uses most of the available nitrate. Its remineralization will increase the $\delta^{15}N$ of
612 ambient nitrate (Casciotti, 2016). However, distinguishing the impact of both processes
613 on sedimentary $\delta^{15}N$ signature might be difficult.
614 Shifts in the position of nutricline depth or in nannoplankton production are
615 indicated by calcareous nannofossil assemblages at Mellala, namely the successive
616 dominance of shallow- and deep-dwellers and the absolute abundance of nannofossils
617 per gram of rock (Fig. 4). Accordingly, the most prominent feature in the $\delta^{15}N$ trend is
618 the decrease occurring at the transition between the Elisa and Mirabile Subzones, at the

619 inception of the negative Pl/To CIE (Fig. 2), simultaneously marking the transition to a
620 shallower nutricline. In the Semicelatum Subzone, $\delta^{15}N$ steadily fluctuates between 1‰
621 and 3‰ (Fig. 2). In the same interval, trophic levels and the nutricline fluctuated, as
622 indicated by nannofossil assemblages (Fig. 4). In contrast, the initial T-OAE CIE interval
623 records very steady $\delta^{15}N$ values of about 2‰, along with very low absolute nannofossil
624 abundances and high proportions of *M. jansae* commonly interpreted as a deep-dweller
625 (for the ecological affinity of taxa, see section 5.1). The very steady $\delta^{15}N$ values may
626 point to a prolonged sourcing of recycled nitrate under stratified water-column conditions.
627 Furthermore, a decline in the marine primary productivity during hyperthermals
628 associated with the Pl/To CIE and the T-OAE CIE may have additionally contributed to
629 preferentially light $\delta^{15}N$ values. The scenario discussed above for the Toarcian events
630 would be most valid for a high-nitrate low-chlorophyll setting, where nitrate utilization is
631 incomplete. Accordingly, primary productivity must have been limited by micronutrients
632 or other environmental parameters. A similar scenario has been daft for the dramatic
633 latest-Rhaetian crisis, where major negative excursions in $\delta^{15}N$ correspond to periods of
634 depressed marine productivity, linked to the development of a stable pycnocline, limited
635 vertical mixing and, finally, limited N availability in surface waters (Schoepfer et al.,
636 2016).
637 Alternatively, in the Algeria basins primary productivity was limited by nitrate
638 availability, and nitrate utilization was essentially complete, leading to no net
639 fractionation. In this scenario, fluctuations in $\delta^{15}N$ reflect the balance of nitrogen fixation
640 and water-column denitrification. This is compatible with the scenario described above
641 on the basis of nannofossil assemblages, of intense stratification and low productivity. In
642 a stratified ocean (especially during the T-OAE CIE interval; Fig. 6A), little nitrate is
643 mixed upward from deep water. Nannofossil abundances likely declined due to a lack of
644 macronutrients in surficial waters, and deep dwellers thrived when nutricline settled deep.
645 Thus, low $\delta^{15}N$ values in sedimentary organic matter was likely due to nitrogen-fixing
646 diazotrophs adding nitrogen to the surface ocean with a low $\delta^{15}N$ value. Conversely, in
647 times of increased vertical mixing of remineralized nitrate, a likely temporarily increased
648 productivity occurred (like in the upper part of the Polymorphum Zone; Fig. 6B). The
649 overall values measured in this study (~2‰) are typical of greenhouse intervals of Earth

650 history, where sedimentary denitrification leads to decreased N recycling and enhanced
651 nitrogen fixation (Algeo et al., 2014).
652
653 *5.3. Palaeoenvironmental conditions in NW Algeria*
654
655 A palaeoenvironmental reconstruction is attempted for the late Pliensbachian-early
656 Toarcian interval, which was studied in the Mellala (Tlemcen Basin) and Raknet El-
657 Kahla (Sahara Basin) sections. Although nannofossil absolute abundance is much
658 higher in Mellala than in Raknet El-Kahla, the trends are similar in both sections, with
659 absolute abundances reaching maxima during the Polymorphum Zone before falling at
660 the beginning of the T-OAE. Another noticeable feature of both sections is represented
661 by the overall high proportions of the species *Mitrolithus jansae*, which is acknowledged
662 to be a taxon with south-Tethys affinities (Bown, 1987; Mattioli et al., 2008) thus
663 proliferating in N-Gondwana basins.
664 Nannofossil absolute abundances as well as the relative abundance of small
665 placolith-coccoliths (i.e., species of the *Lotharingius* genus and Biscutaceae) are much
666 higher in Mellala than in Raknet El-Khala in the early Toarcian Polymorphum Zone (Figs.
667 4 and 5). The nannofossil record from NW Algeria can be thus interpreted in terms of
668 availability of nutrient resources. Higher absolute abundances of all nannofossils and
669 higher proportions of meso-to-eutrophic taxa may likely indicate a higher productivity in
670 Mellala than in Raknet El-Kahla. Interestingly, Raknet El-Khala was located in a small
671 basin bounded by the Sahara Craton to the South and by the Oran Massif to the North.
672 This basin was likely characterized by a restricted water circulation, while the Tlemcen
673 Basin was connected to the open-ocean Tethys to the North. Given the arid regime
674 dominating along the N-Gondwana margin in the Early Jurassic (van de Schootbrugge
675 et al. 2005; Baghli et al., 2020), the Raknet El-Khala section likely lacked significant
676 riverine discharges. Such arid conditions, along with a probable thermal stratification of
677 basin waters, as discussed in Baghli et al. (2020), prevented nutrient replenishment of
678 surface waters where coccolithophore were thriving. The persistent water stratification is
679 further supported by the dominance in nannofossil assemblage of *M. jansae* (proportions
680 usually higher than 50%), which is commonly interpreted as being a deep-dweller,

proliferating in times of stratification and oligotrophy of the upper part of the water column (see section 5.1). The Tlemcen Basin, conversely, was connected by a narrow passage to the North with the Tethys Ocean. The connexion with open-ocean waters might have produced water mixing and, finally, phases of temporary nutrient replenishment in surface waters, favouring proliferation of shallow-dweller species. Such phases alternated with surface water stratification, as indicated by the high proportions of the deep-dweller *M. jansae*, although this latter species is less abundant (in general, proportions lower than 50%) than in Raknet El-Khala. Such fluctuating conditions between stratified and mixed waters, and the subsequent vertical migration of the nutricline, are further supported by the $\delta^{15}N$ record from Mellala and Raknet El-Khala. Thereby, high and although fluctuating $\delta^{15}N$ values in the upper Emaciatum to the lower Polymorphum ammonite Zones may reflect a fluctuating nutricline and re-occuring mixing events, promoting mesotrophic surface waters (Fig. 5B). On the contrary, low and stable $\delta^{15}N$ values during the T-OAE are explained by a deep nutricline, oligotrophic surface waters and low primary productivity (at least for nannoplankton) (Fig. 5A).

Common trends between the two sections are recorded in the two CIE intervals. Within the P-T boundary CIE interval, the absolute abundance of nannofossils is quite high although fluctuating (especially in Mellala). The relative abundances of the meso-eutrophic taxa, such as Biscutaceae, are the highest while the relative abundances of the deep-dweller *M. jansae* and of the incertae sedis *Schizosphaerella* spp. are low in this interval. Such observations suggest relatively high trophic conditions in surface waters during the earliest Toarcian, which are also coherent with low proportions of the deep-dweller *M. jansae*.

Concomitant with the T-OAE negative CIE, also coinciding with anoxia development in several epicontinental basins (McArthur, 2019), extremely low absolute nannofossil abundances are recorded, especially in the Mellala section. In this interval, high proportions of the deep-dweller *M. jansae* occur, while the taxa commonly interpreted as shallow-dwellers (*Schizosphaerella* spp., *Lotharingius* spp. and Biscutaceae) display very low relative abundances. Nannofossil abundance and assemblages are consistent with very low nannofossil production. In a context of the early Toarcian global warming, the negative offset of ~1.5‰ for $\delta^{18}O$ values (*vs*. V-

712 SMOW) observed in NW Algeria compared to European sections has been interpreted
713 as an evidence for higher seawater temperatures along the southern margin of Tethys
714 (Baghli et al., 2020). Accordingly, we attribute this very low nannofossil production to the
715 development of hyper-oligotrophic conditions within the photic zone in NW Algeria
716 basins due to extreme and persistent thermal stratification of the water column.
717
718 *5.4. Comparison between the NW Algeria calcareous nannofossil assemblage and other*
719 *Tethys basins*
720
721 The nannofossil absolute abundances of the Raknet El-Khala section from the
722 Polymorphum Zone are overall lower than those measured in other sections in the
723 western Tethys in the time-equivalent interval. Conversely, Mellala shows nannofossil
724 amounts which are in the same order of magnitude than those recorded in Peniche
725 (Mattioli et al., 2008) or in La Cerradura (Reolid et al., 2014b). In the interval comprised
726 between the upper part of the Polymorphum and the lower half of the Levisoni Zone,
727 time-equivalent to the T-OAE, nannofossil absolute abundances are sensibly low
728 (≤50x10^6 specimens per gram of rock) in NW Algeria as well as in all the areas around
729 the western Tethys (Mattioli et al., 2008; 2009; Reolid et al., 2014b). It is thus likely that
730 extremely low nannofossil palaeo-production occurred in various Tethys areas
731 concomitant with global warming during the T-OAE interval. Calcareous nannofossil
732 abundances and fluxes are the highest in the aftermath of the T-OAE interval in most of
733 the Tethys sections (Mattioli et al., 2009), but in Raknet El-Khala values increased very
734 little in the upper part of the Levisoni Zone.
735 The most relevant difference between calcareous nannofossil assemblages within
736 the Tethys settings is represented by the high abundances of *M. jansae* in NW Algeria.
737 In fact, this taxon occurs very rarely or temporarily disappears in sediments deposited
738 concomitant with the T-OAE in the majority of Tethysn sites (Tremolada et al., 2005;
739 Mattioli et al., 2008), until its LO is recorded in the aftermath of the T-OAE interval
740 (Ferreira et al., 2019). Conversely, in NW Algeria this taxon is dominant (up to 50% of
741 coccoliths) in the T-OAE time-equivalent interval and is still commonly recorded in the
742 upper part of the Levisoni/Serpentinus Zone, before it last occurred at the very base of

743 the Bifrons Zone (Figs. 2 and 4). This peculiar pattern may be interpreted as an
744 evidence of prolonged thermal stratification of marine waters in NW Algeria basins
745 (Baghli et al., 2020). The nutricline likely settled deep in the photic zone under such
746 conditions, producing a palaeo-production decrease of shallow-dweller species and,
747 conversely, promoting proliferation of deep-dwellers. In this view, the NW Algeria basins
748 acted as refugia during the T-OAE, a sort of oases for deep-dwellers that escaped the
749 worst effects of the Toarcian event. Similar narrowly habitable zones, or refuges, within
750 the otherwise lethal Early Triassic world have permitted marine life initially recovered
751 from end-Permian extinction (Godbold et al., 2017).

752 Stratification alone cannot account for the peculiar pattern in NW Algeria records.
753 Stratification has been indeed invoked as the main mechanism favouring anoxia
754 development in many epi-continental basins, especially in the northern margin of NW
755 Europe (Farrimond et al., 1989; Prauss et al., 1991; Bucefalo Palliani et al., 2002;
756 McArthur, 2019). These areas were under the influence of a wet climate, with riverine
757 discharges of fresh waters (van de Schootbrugge et al., 2005; Mattioli et al., 2008;
758 Hermoso and Pellenard, 2014; Philippe et al., 2017) (Fig. 1). Stratification of the water
759 column was thus likely more effective in the northern Tethys margin because it was
760 driven by both thermal and haline gradients. Anoxia reached at times the photic zone, as
761 some Tethys black shales contain organic compounds derived from photosynthesizing
762 bacteria that use hydrogen sulphide (Schouten et al., 2000; Pancost et al., 2004;
763 Schwark and Frimmel, 2004; van Breugel et al., 2006). Intermittent anoxia attaining the
764 deep photic zone is possibly another factor inhibiting the deep-dweller *M. jansae* to
765 develop in epicontinental North Tethys basins (Mattioli et al., 2008).

766 By contrast, previous studies on NW Algeria settings have shown that benthic
767 organisms such as ostracods or foraminifers only temporarily disappeared, likely related
768 to (probable) brief episodes of oxygen depletion of bottom waters of the Sahara Basin
769 (Sebane et al., 2007; Reolid et al., 2012a; Soulimane et al., 2017; Ruebsam et al.,
770 2020a) (Fig. 5B). Benthic foraminifer assemblages are indicative of suboxic conditions in
771 the Tlemcen Basin, where shallow and deep infauna survived the T-OAE conditions,
772 although locally they are present in very low amounts, and only epifauna disappeared

(Reolid et al., 2014) (Fig. 5A). Because of the relevant development of the deep-dweller *M. jansae*, it seems likely that anoxia did not expand upwards in the water column.

Such characteristics are not unique to the Tlemcen Basin. In the Betic Cordillera (Spain) the ichnofacies of the Fuente de la Vidriera section, which was located at the same palaeolatitude as Mellala, revealed oxic or slightly dysoxic bottom waters (Rodriguez-Tovar and Uchman, 2010). The absence of anoxia was further confirmed by the analysis of benthic foraminifers, and by the size of pyrite framboids on the same section (Reolid, 2014a). The Fonte Coberta section in the Lusitanian Basin (Portugal) similarly showed abundant trace fossils in the T-OAE time-equivalent interval. The absence of brachiopods typically reflecting low oxygenation conditions at the sea-bottom allowed Miguez-Salas et al. (2017) to discard the hypothesis of sea floor dysoxia.

The TOC in sediments of most of the sections located along the southern margin of Tethys is commonly as low as 0.5% (or lesser), such as in the Traras section (Algeria; Reolid et al., 2012 a and b; Ruebsam et al., 2020a), Amellago (Morocco, Bodin et al., 2010), La Cerradura (South Spain, Reolid et al., 2014b) and others, which is consistent with the absence of black-shales in this sector of the Tethys. It seems like black-shale development was limited to the NW European regions, mainly due to hydrographic restriction rather than to the consequences of a whole-ocean anoxia (McArthur, 2019).

A recent ocean circulation model developed by Baroni et al. (2018) reconstructed the Toarcian marine current pathway in the western Tethys. In line with the new data from NW Algeria, this model suggests that bottom waters on the southwestern part of the Tethys shelf were mainly oxic during the T-OAE time-equivalent, while those in the north-western basins were mostly anoxic. Modelling shows the presence of a strong clockwise gyre over the European Epicontinental Shelf, which brought oxygenated equatorial waters from the Tethys Ocean to the southern shelf. The northwest branch of the gyre was progressively weakened due to the irregular palaeogeography of the northern shelf, rendering this region prone to ocean stratification and anoxia development. This model also suggests that the Sahara Basin was more affected by restriction of water masses and more prone to bottom water anoxia than the Tlemcen Basin, in which mixing with oxygenated equatorial waters from the Tethys Ocean occurred.

6. Conclusions

A comprehensive study of calcareous nannofossils was conducted in three sections from NW Algeria, namely Djebel Chemarikh and Raknet El-Khala, located in the Sahara Basin, and Mellala, in the Tlemcen Basin. Comparisons with carbon and nitrogen stable isotope data allowed a comprehensive reconstruction of palaeoenvironmental conditions occurring along the N-Gondwana margin concomitant with the Pliensbachian and Toarcian climate perturbations. The main findings of this study are:

• An integrated chrono- and bio-stratigraphic scheme has been established for the first time for NW Algeria. Two negative CIEs are well expressed in the $\delta^{13}C_{carb}$ and $\delta^{13}C_{org}$ records of NW Algeria, namely at the Pliensbachian/Toarcian boundary and concomitant with the T-OAE interval. These new stratigraphic data allow a precise correlation of the two CIEs to isotope records from western Tethys settings.

• The Raknet El-Khala and Mellala sections contain high proportions of the Tethyan coccolith *M. jansae* that was dominant even during the T-OAE CIE. This record is unique in the western Tethys because *M. jansae* is commonly reported to drastically decrease in abundance then to disappear in the aftermath of the T-OAE. It seems that *M. jansae* survived longer in NW Algeria basins, which probably acted as refuge areas.

• Concomitant with the Pliensbachian/Toarcian CIE, nannofossil abundance are quite high in the Mellala section and the assemblage is dominated by coccoliths interpreted as shallow-dwellers, indicative of meso-eutrophic conditions in surface waters, which is corroborated by positive carbon and nitrogen isotope composition. Conversely, during the Toarcian CIE, absolute abundance of all nannofossils but *M. jansae* are extremely low both in Raknet El-Khala and Mellala. We interpret these data as reflecting prolonged stratification and hyper-oligotrophy during the T-OAE in NW Algeria due to thermal stratification. Such an interpretation is compatible with the low $\delta^{15}N$ values and low organic carbon accumulation measured in Mellala.

• Because of the consistent occurrence of *M. jansae* and low TOC values in Mellala, and due to the presence of benthic fauna in the T-OAE interval, it seems that anoxia did

not develop in the Tlemcen Basin. The Sahara Basin was likely more restricted than the Tlemcen Basin and more prone to bottom water anoxia than the Tlemcen Basin, in which mixing with oxygenated equatorial waters from the Tethys Ocean occurred.

Acknowledgements

This paper is a contribution to the IGCP-655 UNESCO project. Funding was provided by IUF to EM. HB benefitted of an Eiffel excellence grant (Campus France). Nannofossil slides are curated at the Collections de Géologie de Lyon (FSL N°: from 768823 to 768856 for Mellala; from 768795 to 768822 for Raknet El-Khala; from 768661 to 768794 for Djebel Chemarikh). WR and LS acknowledge funding by DFG grant Schw554/25 and Schw554/29. This MS benefitted of valuable comments by Shane Schoepfer and an anonymous reviewer. Thomas Algeo is acknowledged for his careful editorial work.

Legend of the figures

Figure 1. (a) Palaeogeographic map of the Western Tethys during the Early Jurassic (modified after Thierry et al., 2000). The main current circulation pattern is shown, as well as the main climatic modes (i.e., arid *vs*. wet) for northern and southern Tethys margins, respectively (modified after Dera and Donnadieu, 2012). (b) map insert showing north-western Algeria during the Toarcian (modified after Elmi and Benshilil, 1987) with the position of the two studied sites.

Figure 2. Litho-, bio-stratigraphic and geochemical data of the studied sections in the Aïn Ouarka sector, Sahara Basin (Djebel Chemarikh and Raknet El-Khala), and in the Tlemcen sector (Mellala). Ammonite biostratigraphy for Djebel Chemarikh and Raknet El-Khala sections is after Mekahli (1998), for the Mellala section it is after Elmi et al. (2006). In Elmi et al. (2006), the base of the Toarcian in Mellala section was initially placed in the bed 38, bearing the earliest *Paltarpites paltus* (Buckman) but without *Eodactylites*. Bed 40 has yielded several *Dactylioceras* (*Eodactylites*) *polymorphum* (Fucini), *D*. (*E*.) *mirabile* (Fucini) and *D*. (*E*.) *pseudocommune* (Fucini) (corresponding to

866 "1. first *Eodactylites*" in the figure). *Eodactylites* becomes abundant, especially in bed 44
867 (our "2. principal bed with *Eodactylites*"). According to the ratified GSSP at Peniche,
868 Portugal, the base of the Toarcian Stage is marked by the concomitant first occurrence
869 of several *Eodactylites*, such as *D*. (*E*.) *simplex*, *D*. (*E*.) *pseudocommune* and *D*. (*E*.)
870 *polymorphum*. Accordingly, in this paper we have placed the base of the Toarcian stage
871 at Mellala to the bed 40 of Elmi et al. (2006). Stable carbon and nitrogen isotope values,
872 and wt.%TOC for the Raknet El-Khala section are after Reolid et al. (2012b) and
873 Ruebsam et al. (2020a). For the Mellala section, we present new stable isotope (bulk
874 carbonate carbon, bulk organic carbon, nitrogen) and organic carbon content (wt.%TOC).
875 Nannofossil biostratigraphy allowed the establishment of nannofossil zones for the NW
876 Algeria sector, according to the bio-chronology of Mattioli and Erba (1999) and Ferreira
877 et al. (2019). Note the different vertical scale: 1 scale bar = 10 meters at Djebel
878 Chemarikh; 1 bar = 1 meter at Raknet El-Khala and Mellala.
879
880 Figure 3. Calcareous nannofossil absolute (specimens per gram of rock) and relative
881 (percentage) abundance in the Ratnek El-Kahla section. The percentages of the main
882 coccolith taxa (normalized to total coccolith content) and of the *incertae sedis*
883 *Schizosphaerella* (normalized to nannofossil content) are shown. The volume of 30
884 specimens of *M. jansae* per sample (except for the lowermost sample) has been
885 calculated on the basis of images captured with the software ImageJ©. The black line
886 represents average values, grey lines shows the standard deviation as calculated with
887 PAST.
888
889 Figure 4. Calcareous nannofossil absolute (specimens per gram of rock) and relative
890 (percentage) abundance in the Mellala section. The percentages of the main coccolith
891 taxa (normalized to over total coccolith content) and of the *incertae sedis*
892 *Schizospharella* (normalized to over total nannofossil content) are shown.
893
894 Figure 5. Schematic representation of palaeoenvironmental conditions prevailing within
895 the two NW Algeria basins during the Toarcian CIE corresponding to the T-OAE interval
896 (A) and to the Polymorphum Zone, prior to the T-OAE interval (B). Upward and

downward arrows indicate increase or decrease in organism abundances. N_2 fixation by diazotroph cyanobacteria is shown. ~~In particular,~~ (A) Calcareous nannofossiles interpreted as being shallow-dwellers are rare during the T-OAE interval especially at Raknet El-Khala, while deep-dwellers were relatively more abundant. Anoxia at Raknet El-Khala developed both in bottom and pore-waters. At Mellala, infauna foraminifera were present throughout the T-OAE, although in low proportions, and only epifauna disappeared (after Reolid et al., 2014). (B) Some of the highest abundance of both shallow- and deep-dweller nannofossil taxa are recorded in the upper part of the Polymorphum Zone, corresponding to periods of vertical mixin and remineralization of nitrates. See the text for more explanations.

Tables 1 to 3. Distribution chart of calcareous nannofossils in the three studied sections.

Plates 1 and 2. Selected nannofossil taxa from the studied sections. The scale bar is 2 µm.

References

Aït Ouali, R., 1991. Le rifting des Monts des Ksour au Lias. Organisation du bassin, diage- nèse des assises carbonatées, place dans les ouvertures mésozoiques au Maghreb. Unpublished PhD Thesis Univ. STHB Alger, 298 pp..

Algeo, T.J., Meyers, P.A., Robinson, R.S., Rowe, H. and Jiang, G.Q., 2014. Icehouse-greenhouse variations in marine denitrification. Biogeosciences, 11(4), 1273–1295.

Ameur, M., 1999. Histoire d'une plate-forme carbonatée de la marge Sud-Téthysienne: L'autochtone des Traras (Algérie occidentale) du Trias Supérieur jusqu'au Bathonien Moyen. Docum. Lab. Géol. Lyon, n°150,1999. 1–399.

Baghli, H., Mattioli, E., Spangenberg, J.E., Bensalah, M., Arnaud-Godet, F., Pittet, B., Suan, G., 2020. Early Jurassic climatic trends in the south-Tethyan margin. Gondwana Research. https://doi.org/10.1016/j.gr.2019.06.016

Baroni, I.R., Pohl, A., van Helmond, N.A.G.M., Papadomanolaki, N.M., Coe, A.L., Cohen, A.S., van de Schootbrugge, B., Donnadieu, Y., Slomp, C.P., 2018. Ocean

928 Circulation in the Toarcian (Early Jurassic): A Key Control on Deoxygenation and
929 Carbon Burial on the European Shelf. Paleoceanography and Paleoclimatology, 33,
930 994–1012. https://doi.org/10.1029/2018PA003394
931 Beaufort, L., Barbarin, N., Gally, Y., 2014. Optical measure- ments to determine the
932 thickness of calcite crystals and the mass of thin carbonate particles such as
933 coccoliths. Nature Protocols 9, 633–642.
934 Bodin, S., Mattioli, E., Fröhlich, S., Marshall, J.D., Boutib, L., Lahsini, S., Redfern, J.,
935 2010. Toarcian carbon isotope shifts and nutrient changes from the Northern
936 margin of Gondwana (High Atlas, Morocco, Jurassic): palaeoenvironmental
937 implications. Palaeogeography Palaeoclimatology Palaeoecology 297, 377–390.
938 https:// doi.org/10.1016/j.palaeo.2010.08.018.
939 Bougeault, C., Pellenard, P., Deconinck, J.F., Hesselbo, S.P., Dommergues, J.L.,
940 Bruneau, L., Cocquerez, T., Laffont, R., Huret, E., Thibault, N.R., 2017. Climatic
941 and palaeoceanographic changes during the Pliensbachian (Early Jurassic)
942 inferred from clay mineralogy and stable isotope (CO) geochemistry (NW Europe).
943 Global and Planetary Change 149, 139–152.
944 Bour, I., Mattioli, E., Pittet, B., 2007. Nannofacies analysis as a tool to reconstruct
945 palaeoenvironmental changes during the Early Toarcian anoxic event.
946 Palaeogeography, Palaeoclimatology, Palaeoecology 249, 58–79.
947 Bown, P.R., 1987. Taxonomy, evolution and biostratigraphy of Late Triassic-early
948 Jurassic calcareous nannofossils. Special Papers in Paleontology 38, 1–118.
949 Bown, P.R., Cooper, M.K.E., 1998. Jurassic. In: Bown, P. R. (Ed.), Calcareous
950 Nannofossil Biostratigraphy, British Micropalaeontological Society Series.
951 Chapman and Hall/Kluwer Academic Publishers, London, 86–131.
952 Bracène, R., Frizon de Lamotte, D., 2002. The origin of intraplate deformation in the
953 Atlas system of western and central Algeria: from Jurassic rifting to Cenozoic–
954 Quaternary inversion. Tectonophysics 357, 207–226.
955 https://doi.org/10.1016/S0040-1951(02)00369-4
956 Brand, W.A., Coplen, T.B., Vogl, J., Rosner, M., Prohaska, T., 2014. Assessment of
957 international reference materials for isotope-ratio analysis. Pure and Applied
958 Chemistry 8866, 425–467.

959 Brandes, J.A., Devol, A.H., 2002. A global marine-fixed nitrogen iso- topic budget:
960 implications for Holocene nitrogen cycling, Glob. Biogeochem. Cy., 16, 1120,
961 doi:10.1029/2001GB001856, 1–14, 2002.
962 Breugel, van, Y., Baas, M., Schouten, S., Mattioli, E., Sinninghe-Damste, J.S., 2006.
963 Isorenieratane record in black shales from the Paris Basin, France: Constraints on
964 recycling of respired CO2 as a mechanism for negative carbon isotope shifts
965 during the Toarcian oceanic anoxic event. Paleoceanography 21, PA4220,
966 doi:10.1029/2006PA001305, 2006.
967 Bucefalo-Palliani, R., Mattioli, E., 1998. High resolution potential of the calcareous
968 nannofossil and dinoflagellate cyst integrated biostratigraphy in the Lower Jurassic
969 (Late Pliensbachian-Lower Toarcian) of Central Italy. Journal of Micropaleontology
970 17, 153-172.
971 Bucefalo-Palliani, R., Mattioli, E., Riding, J., 2002. The response of marine
972 phytoplankton and sedimentary organic matter to the early Toarcian (Lower
973 Jurassic) oceanic anoxic event in northern England. Marine Micropaleontology 46,
974 223-245.
975 Casciotti, K.L., 2016. Nitrogen and Oxygen Isotopic Studies of the Marine Nitrogen
976 Cycle. Annu. Rev. Mar. Sci. 8, 379-407.
977 Claps, M., Erba, E., Masetti, D., Melchiorri, F., 1995. Milankovitch-type cycles recorded
978 in Toarcian black shales from the Belluno Trough (Southern Alps Italy). Memorie di
979 Scienze Geologiche de Padova 47, 179–188.
980 Deconinck, J.F., Hesselbo, S.P., Pellenard, P., 2019. Climatic and sea-level control of
981 Jurassic (Pliensbachian) clay mineral sedimentation in the Cardigan Bay Basin,
982 Llanbedr (Mochras Farm) borehole Wales. Sedimentology 66, 2769–2783.
983 Dera, G., Donnadieu, Y., 2012. Modeling evidences for global warming, Arctic seawater
984 freshening, and sluggish oceanic circulation during the Early Toarcian anoxic event.
985 Paleoceanography, 27, 1–15.
986 Elmi, S., Alméras, Y., 1984. Physiography, palaeotectonics and palaeoenvironments as
987 controls of changes in ammonite and brachiopod communities (an example from
988 the Early and Middle Jurassic of Western Algeria). Palaeogeography
989 Palaeoclimatology Palaeoecology 47, 347–360.

990 Elmi, S., Benshilil, K., 1987. Relations entre la structuration tectonique, la composition
991 des peuplements et l'Évolution : exemple du Toarcien du Moyen Atlas mÉridional
992 (Maroc). Bull. Soc. Paleontol. Ital 26, 47–62.
993 Elmi, S., Alméras, Y., Bassoullet, J.P., Boutakiout, M., Benhamou, M., Marok, A.,
994 Mekahli, L., Mekkaoui, A., Mouterde, R., 1998. Stratigraphic and palaeogeographic
995 survey of the Lower and Middle Jurassic along a north–south transect in western
996 Algeria. Mémoires Mus. Natl. d'Hist. Nat. 179, 145–211.
997 Elmi, S., Marok, A., Sebane, A., Alméras, Y., 2006. Importance of the Mellala section
998 (Traras Mountains, northwestern Algeria) for the correlation of the Pliensbachian-
999 Toarcian boundary. Volumina Jurassica VII, 37–45.
1000 Erba, E., 2004. Calcareous nannofossils and Mesozoic oceanic anoxic events. Marine
1001 Micropaleontology 52, 85–106.
1002 Farrimond, P., Eglinton, G., Brassell, S.C., Jenkyns, H.C., 1989. Toarcian anoxic event
1003 in Europe: an organic geochemical study. Mar. Petrol. Geol., 6, 136–147.
1004 Fatela, F., Taborda, R., 2002. Confidence limits of species proportions in microfossil
1005 assemblages. Marine Micropaleontology 45, 169-174.
1006 Favre, P., Stampfli, G., Wildi, W., 1991. Jurassic sedimentary record and tectonic
1007 evolution of the northwestern corner of Africa. Palaeogeography Palaeoclimatology
1008 Palaeoecology 87, 53-73.
1009 Ferreira, J., Mattioli, E., Sucherás-Marx, B., Giraud, F., Duarte, L.V., Pittet, B., Suan, G.,
1010 Hassler, A., Spangenberg, J.E., 2019. Western Tethys Early and Middle Jurassic
1011 calcareous nannofossil biostratigraphy. Earth Science Review.
1012 https://doi.org/10.1016/j.earscirev.2019.102908
1013 Fraguas, A., 2014. *Crepidolithus cantabriensis* nov. sp., a new calcareous nannofossil
1014 (Prymnesiophyceae) from the Lower Jurassic of northern Spain. Geobios 47, 31–
1015 38. http://dx.doi.org/10.1016/j.geobios.2013.10.004
1016 Frizon de Lamotte, D., Leturmy, P., Missenard, Y., Khomsi, S., Ruiz, G., Saddiqi, O.,
1017 Guillocheau, F., Michard, A., 2009. Mesozoic and Cenozoic vertical movements in
1018 the Atlas system (Algeria, Morocco, Tunisia): an overview. Tectonophysics 475, 9–
1019 28.

1020 Godbold, A., Schoepfer. S., Shen, S., Henderson, C.M., 2017. Precarious ephemeral
1021 refugia during the earliest Triassic. Geology 45(7), 607–610. doi:10.1130/G38793.1
1022 Gómez, J.J., Goy, A., 2011. Warming-driven mass extinction in the Early Toarcian (Early
1023 Jurassic) of northern and central Spain. Correlation with other time-equivalent
1024 European sections. Palaeogeography Palaeoclimatology Palaeoecology 306, 176–
1025 195.
1026 Gómez, J.J., Goy, A., Canales, M.L., 2008. Seawater temperature and carbon isotope
1027 variations in belemnites linked to mass extinction during the Toarcian (Early
1028 Jurassic) in Central and Northern Spain. Comparison with other European sections.
1029 Palaeogeography Palaeoclimatology Palaeoecology 258, 28–58. https://doi.org/10.
1030 1016/j.palaeo.2007.11.005.
1031 Guex, J., Morard, A., Bartolini, A., Morettini, E., 2001. Découverte d'une importante
1032 lacune stratigraphique à la limite Domérien-Toarcien: implications paléo-
1033 océanographiques. Bull. Soc. Vaud. Sci. Nat., 345, 277–284.
1034 Gruber, N., 2008. Chapter 1 - The marine nitrogen cycle: Overview and challenges. In:
1035 Capone, D.G., Bronk, D.A., Mulholland, M.R., Carpenter, E.J., (Eds.). Nitrogen in
1036 the marine environment. Elsevier, p. 1-50.
1037 Hammer, Ø., Harper, D.A.T., Ryan, P.D., 2001. PAST: paleontological statistics software
1038 package for education and data analysis. Palaeontol. Electron. 4, 1–9.
1039 Harries, P.J., Little, C.T.S., 1999. The early Toarcian (Early Jurassic) and the
1040 Cenomanian–Turonian (Late Cretaceous) mass extinctions: similarities and
1041 contrasts. Palaeogeography Palaeoclimatology Palaeoecology 154, 39–66.
1042 Hermoso, M., Pellenard, P., 2014. Continental weathering and climatic changes inferred
1043 from clay mineralogy and paired carbon isotopes across the early to middle
1044 Toarcian in the Paris Basin. Palaeogeography, Palaeoclimatology, Palaeoecology
1045 399, 385-393.
1046 Hermoso, M., Minoletti, F., Pellenard, P., 2013. Black shale deposition during Toarcian
1047 super-greenhouse driven by sea level. Clim. Past 9, 2703–2712.
1048 Hesselbo, S.P., Gröcke, D.R., Jenkyns, H.C., Bjerrum, C.J., Farrimond, P., Morgans Bell,
1049 H.S., Green, O.R., 2000. Massive dissociation of gas hydrate during a Jurassic
1050 oceanic anoxic event. Nature 406, 392–395. https://doi.org/10.1038/35019044.

1051 Hesselbo, S.P., Jenkyns, H.C., Duarte, L.V., Oliveira, L.C.V., 2007. Carbon-isotope
1052 record of the Early Jurassic (Toarcian) oceanic anoxic event from fossil wood and
1053 marine carbonate (Lusitanian Basin, Portugal). Earth and Planetary Science
1054 Letters 253, 455–470. https://doi.org/10.1016/J.EPSL.2006.11.009.
1055 Jenkyns, H.C., 1988. The early Toarcian (Jurassic) event: stratigraphy, sedimentary,
1056 and geochemical evidence. American Journal of Science 288, 101–151. https://doi.
1057 org/10.2475/ajs.288.2.101.
1058 Jenkyns, H.C., Clayton, C.J., 1997. Lower Jurassic epicontinental carbonates and
1059 mudstones from England and Wales: chemostratigraphic signals and the early
1060 Toarcian anoxic event. Sedimentology 44, 687–706. https://doi.org/10.1046/j.1365-
1061 3091.1997.d01-43.x.
1062 Kemp, D.B., Coe, A.L., Cohen, A.S., Schwark, L., 2005. Astronomical pacing of methane
1063 release in the Early Jurassic period. Nature 437, 396–399.
1064 Korte, C., Hesselbo, S.P., 2011. Shallow marine carbon and oxygen isotope and
1065 elemental records indicate icehouse-greenhouse cycles during the Early Jurassic.
1066 26, 1–18. https://doi.org/10.1029/2011PA002160.
1067 Li, Q., McArthur, J.M., Atkinson, T.C., 2012. Lower Jurassic belemnites as indicators of
1068 palaeo-temperature. Palaeogeography Palaeoclimatology Palaeoecology 315–316,
1069 38–45. https://doi.org/10.1016/j.palaeo.2011.11.006.
1070 Littler, K., Hesselbo, S.P., Jenkyns, H.C., 2009. A carbon-isotope perturbation at the
1071 Pliensbachian-Toarcian boundary: evidence from the Lias Group, NE England.
1072 Geological Magazine 147, 181–192. https://doi.org/10.1017/S0016756809990458
1073 Macchioni, F., Cecca, F., 2002. Biodiversity and biogeography of middle–late liassic
1074 ammonoids: implications for the early Toarcian mass extinction. Geobios 35, 165–
1075 175. https://doi.org/10.1016/S0016-6995(02)00057-8.
1076 Mattioli, E., Erba, E., 1999. Biostratigraphic syntesis of calcareous nannofossil events in
1077 the Tethyan Jurassic. Rivista Italiana di Paleontologia e Stratigrafia 105(3), 343-
1078 376.
1079 Mattioli, E., Pittet, B., 2004. Spatial and temporal distribution of calcareous nannofossils
1080 along a proximal-distal transect in the Umbria-Marche basin (Lower Jurassic; Italy).
1081 Palaeogeography, Palaeoclimatology, Palaeoecology 205, 295-316.

1082 Mattioli, E., Pittet, B., Suan, G., Mailliot, S., 2008. Calcareous nannoplankton changes
1083 across the early Toarcian oceanic anoxic event in the western Tethys.
1084 Paleoceanography 23, 1–17. https://doi.org/10.1029/2007PA001435.
1085 Mattioli, E., Pittet, B., Petitpierre, L., Mailliot, S., 2009. Dramatic decrease of the pelagic
1086 carbonate production by nannoplankton across the Early Toarcian Anoxic Event
1087 (T-OAE). Global and Planetary Changes 65, 134-145.
1088 doi:10.1016/j.gloplacha.2008. 10.018
1089 Mattioli, E., Plancq, J., Boussaha, M., Duarte, L.V., Pittet, B., 2013. Calcareous
1090 nannofossil biostratigraphy: new data from the Lower Jurassic of the Lusitanian
1091 Basin. Comunicações Geológicas (2013) 100, Especial I, 69-76 ISSN: 0873-948X;
1092 e-ISSN: 1647-581X
1093 McArthur, J.M.Y., Donovan, D.T., Thirlwall, M.F., Fouke, B.W., 2000. Strontium isotope
1094 profile of the early Toarcian (Jurassic) oceanic anoxic event, the duration of
1095 ammonite biozones, and belemnite palaeotemperatures. Earth and Planetary
1096 Science Letters 179, 269–285. https://doi.org/10.1016/S0012-821X(00)00111-4.
1097 McArthur, J. M., Algeo, T. J., van de Schootbrugge, B., Li, Q., Howarth, R. J., 2008.
1098 Basinal restriction, black shales, Re-Os dating, and the Early Toarcian (Jurassic)
1099 oceanic anoxic event. Paleoceanography 23 (4).
1100 McArthur, J.M., 2019. Early Toarcian black shales: A response to an oceanic anoxic
1101 event or anoxia in marginal basins. Chemical Geology 522, 71-83,
1102 https://doi.org/10.1016/j.chemgeo.2019.05.028
1103 Mekahli, L., 1988. Le jurassique inferieur et moyen de la partie occidentale du horst de
1104 Rhar-Roubane (Tlemcen, Algerie Occidentale) : stratigraphie, sedimentologie et
1105 cadre dynamique. Thèse de Magistère. Université d'Oran, pp. 1–245 Unpublished.
1106 Mekahli, L., Elmi, S., Benhamou, M., 2004. Biostratigraphy, sedimentology and tectono-
1107 eustatic events of the Lower and Middle Jurassic of the Ksour Mountains (Western
1108 Saharian Atlas, Southern Algeria). 32nd International Geological Congress 5, Field
1109 Trip Guide Book-P 52, Florence, p. 28.
1110 Menini, A., Mattioli, E., Spangenberg, J. E., Pittet, B., Suan, G., 2019. New calcareous
1111 nannofossil and carbon isotope data for the Pliensbachian/Toarcian boundary

(Early Jurassic) in the western Tethys and their paleoenvironmental implications. Newsletters on Stratigraphy 52, 173-196, doi:10.1127/nos/2018/0476 (2019).

Menini, A., Mattioli, E., Hesselbo, S.P., Ruhl, M. Suan, G., 2021. Primary v. carbonate production in the Toarcian, a case study from the Llanbedr (Mochras Farm) borehole, Wales). From: Reolid, M., Duarte, L. V., Mattioli, E. and Ruebsam, W. (Eds) Carbon Cycle and Ecosystem Response to the Jenkyns Event in the Early Toarcian (Jurassic). Geological Society, London, Special Publications, 514, https://doi.org/10.1144/SP514-2021-74.

Miguez-Salas, O., Rodríguez-Tovar, F.J., Duarte, L.V., 2017. Selective incidence of the Toarcian oceanic anoxic event on macroinverte- brate marine communities: a case from the Lusitanian basin, Portugal. Lethaia 50, 548–560.

Molfino, B., McIntyre, A., 1990. Precessional forcing of nutricline dynamics in the equatorial Atlantic. Science 249, 766–769.

Moore, D.M., Reynolds, R.C., 1997. X-ray Diffraction and the Identification and Analysis of 679 Clay Minerals. Oxford University Press, New York, 400 pp..

Müller, T., Price, G.D., Bajnai, D., Nyerges, A., Kesjár, D., Raucsik, B., Varga, A., Judik, K., Fekete, J., May, Z., Pálfy, J., 2017. New multiproxy record of the Jenkyns Event (also known as the Toarcian Oceanic Anoxic Event) from the Mecsek Mountains (Hungary): Differences, duration and drivers Sedimentology 64, 66–86. https://doi.org/10.1111/sed.12332.

Olivier, N., Pittet, B., Mattioli, E., 2004. Palaeoenvironmental control on sponge-reefs and contemporaneous deep-shelf marl-limestone deposition (Late Oxfordian, southern Germany). Palaeogeography, Palaeoclimatology, Palaeoecology 212, 233-263.

Pancost, R. D., Crawford, N., Magness, S., Turner, A., Jenkyns, H. C., & Maxwell, J. R. (2004). Further evidence for the development of photic-zone euxinic conditions during Mesozoic Oceanic Anoxic Events. Journal of the Geological Society of London, 161(3), 353–364.

Philippe, M., Puijalon, S., Suan, G., Mousset, S., Thévenard, F., Mattioli, E., 2017. The palaeolatitudinal distribution of fossil wood genera as a proxy for European

Jurassic terrestrial climate. Palaeogeography, Palaeoclimatology, Palaeoecology 466, 373–381.

Pittet, B., Mattioli, E., 2002. The carbonate signal and calcareous nannofossil distribution in an Upper Jurassic section (Balingen-Tieringen, Late Oxfordian, southern Germany). Palaeogeography, Palaeoclimatology, Palaeoecology 179, 71-96.

Pittet, B., Suan, G., Lenoir, F., Duarte, L.V., Mattioli, E., 2014. Carbon isotope evidence for sedimentary discontinuities in the lower Toarcian of the Lusitanian Basin (Portugal): sea level changes at the onset of the Oceanic Anoxic Event. Sedimentary Geology 303, 1-14.

Prauss, M., Ligouis, B., Luterbacher, H., 1991. Organic matter and palynomorphs in the 'Posidonienschiefer' (Toarcian, Lower Jurassic) of southern Germany, in Modern and Ancient Continental Shelf Anoxia. In: R.V. Tyson and T.H. Pearson (Eds.), Geological Society Special Publication London, 58, 335–352.

Price, G.D., Baker, S.J., VanDeVelde, J., Clémence, M.-E., 2016. High-resolution carbon cycle and seawater temperature evolution during the Early Jurassic (Sinemurian- Early Pliensbachian). Geochemistry, Geophysics, Geosystems 17, 3917–3928. https://doi.org/10.1002/2016GC006541.

Reggiani, L., Mattioli, E., Pittet, B., Duarte, L.V., Veiga de Oliveira, L.C., Comas-Rengifo, M.J., 2010. Pliensbachian (Early Jurassic) calcareous nannofossils from the Peniche section (Lusitanian Basin, Portugal): A clue for palaeoenvironmental reconstructions Marine Micropaleontology doi:10.1016/j.marmicro.2010.02.002

Remírez, M.N., Algeo, T.J., 2020a. Paleosalinity determination in ancient epicontinental seas: A case study of the T-OAE in the Cleveland Basin (UK). Earth-Science Reviews, 201, p.103072. doi.org/10.1016/j.earscirev.2020.103283

Remírez, M.N., Algeo, T.J., 2020b. Carbon-cycle changes during the Toarcian (Early Jurassic) and implications for regional *versus* global drivers of the Toarcian oceanic anoxic event. Earth-Science Reviews, p. 103283. doi.org/10.1016/j.earscirev.2019.103072

Reolid, M., Rodríguez-Tovar, F.J., Marok, A., Sebane, A., 2012a. The Toarcian Oceanic Anoxic Event in the Western Saharan Atlas, Algeria (North African Paleomargin):

Role of Anoxia and Productivity. Geological Society of America Bulletin 124, 1646–1664. https://doi.org/10.1130/B30585.1

Reolid, M., Sebane, A., Rodríguez-Tovar, F.J., Marok, A., 2012b. Foraminiferal morphogroups as a tool to approach the Toarcian Anoxic Event in the Western Saharan Atlas (Algeria). Palaeogeography Palaeoclimatology Palaeoecology 323–325, 87–99.

Reolid M., Marok A., Sebane A., 2014a. Foraminiferal assemblages and geochemistry for interpreting the incidence of Early Toarcian environmental changes in North Gondwana palaeomargin (Traras Mountains, Algeria). Journal of African Earth Sciences 95,105–122.

Reolid, M., Mattioli, E., Nieto, L.M., Rodríguez-Tovar, F.J., 2014b. The Early Toarcian Oceanic Anoxic Event in the External Subbetic (Southiberian Palaeomargin, Westernmost Tethys): Geochemistry, nannofossils and ichnology. Palaeogeography, Palaeoclimatology, Palaeoecology 411, 79-94.

Rita, P., Reolid, M., Duarte, L.V., 2016. Benthic foraminiferal assemblages record major environmental perturbations during the Late Pliensbachian–Early Toarcian interval in the Peniche GSSP, Portugal. Palaeogeography Palaeoclimatology Palaeoecology 454, 267–281.

Ritter E., 1902. Le Djebel Amour et les Monts des Oulad Naïl. Bull. Serv. Carte Géol. Algérie, 2° série, n°3, 100 p., 4 pl. h.t.

Rocha, da, R., Mattioli, E., Duarte, L.V., Pittet, B., Elmi, S., Mouterde, R., Cabral, M.C., Comas-Rengifo, M.J., Gómez, J.J., Goy, A., Hesselbo, S.P., Jenkyns, H.C., Littler, K., Mailliot, S., Veiga de Oliveira, L.C., Osete, M.L., Perilli, N., Pinto, S., Ruget, C. Suan, G., 2016. Base of the Toarcian Stage of the Lower Jurassic defined by the Global Boundary Stratotype Section and Point (GSSP) at the Peniche section (Portugal). Episodes 39, 460-481.

Rodríguez-Tovar, F.J., Uchman, A., 2010. Ichnofabric evidence for the lack of bottom anoxia during the Lower Toarcian oceanic anoxic event (T-OAE) in the Fuente de la Vidriera section, Betic Cordillera, Spain. Palaios 25, 576–587, doi:10.2110/palo.2009.p09-153r.

1202 Röhl, H.J., Schmidt-Röhl, A., Oschmann, W., Frimmel, A., Schwark, L., 2001. The
1203 Posidonia Shale (Lower Toarcian) of SW-Germany: an oxygen-depleted
1204 ecosystem controlled by sea level and palaeoclimate. Palaeogeogr. Palaeoclimatol.
1205 Palaeoecol. 165, 27–52.
1206 Rosales, I., Quesada, S., Robles, S., 2004, Paleotemperature variations of Early
1207 Jurassic seawater recorded in geochemical trends of belemnites from the Basque-
1208 Cantabrian Basin, northern Spain. Palaeogeography, Palaeoclimatology,
1209 Palaeoecology 203, 253–275.
1210 Roth, P.H., 1984. Preservation of calcareous nannofossils and fine-grained carbonate
1211 particles in mid-Cretaceous sediments from the southern Angola Basin. In: Hay, W.
1212 W. (Ed.), Initial Reports of Deep Sea Drilling Project 75. U. S. Government Printing
1213 Office, Washington, pp. 651–655.
1214 Ruebsam, W., Al-Husseini, M., 2020. Calibrating the Early Toarcian (Early Jurassic) with
1215 stratigraphic black holes (SBH). Gondwana Research 82, 317–336.
1216 Ruebsam, W., Müller, T., Kovács, J., Pálfy, J., Schwark, L., 2018. Environmental
1217 response to the early Toarcian carbon cycle and climate perturbations in the
1218 northeastern part of the West-Tethys shelf. Gondwana Res. 59, 144–158.
1219 Ruebsam, W., Reolid, M., Marok, A., Schwark, L., 2020a. Drivers of benthic extinction
1220 during the early Toarcian (Early Jurassic) at the northern Gondwana paleomargin:
1221 Implications for paleoceanographic conditions. Earth-Science Reviews 203,
1222 103177.
1223 Ruebsam, W., Reolid, M., Schwark, L., 2000b. $\delta^{13}C$ of terrestrial vegetation records
1224 Toarcian CO_2 and climate gradients. Nature Scientific Reports 10, 117.
1225 Ruebsam, W., Reolid, M., Sabatino, N., Masetti, D., Schwark, L., 2020c. Molecular
1226 paleothermometry of the early Toarcian climate perturbation. Global and Planetary
1227 Change. doi.org/10.1016/j.gloplacha.2020.103351
1228 Sabatino, N., Neri, R., Bellanca, A., Jenkyns, H., Baudin, F., Parisi, G., Masetti, D., 2009.
1229 Carbon-isotope records of the Early Jurassic (Toarcian) oceanic anoxic event from
1230 the Valdorbia (Umbria–Marche Apennines) and Monte Mangart (Julian Alps)
1231 sections: palaeoceanographic and stratigraphic implications. Sedimentology 56,
1232 1307–1328.

1233 Schlachter, T.A., Connolly, R.M., 2014. Effects of acid treatment on carbon and nitrogen
1234 stable isotope ratios in ecological samples: a review and synthesis. Methods Ecol.
1235 Evol. 5, 541–550.
1236 Schootbrugge, van de, B., Bailey, T.R., Rosenthal, Y., Katz, M.E., Wright, J.D., Miller,
1237 K.G., Feist-Burkhardt, S., Falkowski, P. G., 2005. Early Jurassic climate change
1238 and the radiation of organic-walled phytoplankton in the Tethys Ocean.
1239 Paleobiology 31, 73–97.
1240 Schouten, S., Van Kaam-Peters, H.M.E., Rijpstra, W.I.C., Schoell, M., Sinninghe
1241 Damsté, J.S., 2000. Effects of an oceanic anoxic event on the stable carbon
1242 isotopic compo- sition of Early Toarcian carbon. American Journal of Sciences 300,
1243 1–22.
1244 Schwark, L., Frimmel, A., 2004. Chemostratigraphy of the Posidonia black shale, SW-
1245 Germany II. Assessment of extent and persistence of photic-zone anoxia using aryl
1246 isoprenoid distributions. Chemical Geology 206, 231–248. https://doi.org/10.1016/j.
1247 chemgeo.2003.12.008.
1248 Schoepfer, S.D., Algeo, T.J., Ward, P.D., Williford, K.H., Haggart, J.W., 2016. Testing
1249 the limits in a greenhouse ocean: Did low nitrogen availability limit marine
1250 productivity during the end-Triassic mass extinction?. Earth and Planetary Science
1251 Letters 451, 138-148. doi.org/10.1016/j.epsl.2016.06.050
1252 Sebane, A., Marok, A., Elmi, S., 2007. Évolution des peuplements de foraminifers
1253 pensant la crise toarcienne à l'exemple des données des Monts des Ksour (Atlas
1254 Saharien Occidental, Algérie). Comptes Rendus Palévol. 6, 189–196,
1255 doi:10.1016/j.crpv.2006.10.002.
1256 Soulimane, C., Reolid, M., Marok, A., 2017. Ostracod assemblages from the uppermost
1257 Pliensbachian and Lower Toarcian of the Traras Mountains (Tlemcen Domain,
1258 north Algeria). Arabian Journal of Geosciences 10, 393.
1259 https://doi.org/10.1007/s12517-017-3180-0
1260 Suan, G., Mattioli, E., Pittet, B., Mailliot, S., Lécuyer, C., 2008. Evidence for major
1261 environmental perturbation prior to and during the Toarcian (Early Jurassic)
1262 oceanic anoxic event from the Lusitanian Basin, Portugal. Paleoceanography 23,
1263 1–14. https://doi.org/10.1029/2007PA001459.

1264 Suan, G., Mattioli, E., Pittet, B., Lécuyer, C., Suchéras-Marx, B., Duarte, L.V., Philippe,
1265 M., Reggiani, L., Martineau, F., 2010. Secular environmental precursors to Early
1266 Toarcian (Jurassic) extreme climate changes. Earth and Planetary Science Letters
1267 290, 448–458. https://doi.org/10.1016/J.EPSL.2009.12.047.
1268 Suan, G., van de Schootbrugge, B., Adatte, T., Fiebig, J., Oschmann, W., 2015.
1269 Calibrating and magnitude of the Toarcian carbon cycle perturbation.
1270 Paleoceanography 30, PA2758.
1271 Tremolada, F., Van de Schootbrugge, B. Erba, E., 2005. Early Jurassic
1272 schizosphaerellid crisis in Cantabria, Spain: Implications for calcification rates and
1273 phytoplankton evolution across the Toarcian oceanic anoxic event.
1274 Paleoceanography 20, PA2011, doi:10.1029/2004PA001120.
1275 Vafeiadou, A.M., Helena, A., De Troch, M., Moens, T., 2013. Sample acidification effects
1276 on carbon and nitrogen stable isotope ratios of macrofauna from a Zostera noltii
1277 bed. Mar. Freshw. Res. 64, 741–745.
1278 Visentin, S., Faucher, G., Mattioli, E. Erba, E., 2020. Taxonomic revision of genus
1279 Carinolithus (Early - Middle Jurassic) based on morphometric analyses and
1280 diagenesis observations: Implications for biostratigraphy and evolutionary trends.
1281 Marine Micropaleontology. https://doi.org/10.1016/j.marmicro.2020.101950
1282 Wignall, P.B., 2001. Large igneous provinces and mass extinctions. Earth Science
1283 Reviews 53, 1–33. https://doi.org/10.1016/S0012-8252(00)00037-4.
1284 Wilmsen, M., Neuweiler, F., 2008. Biosedimentology of the Early Jurassic post-extinction
1285 carbonate depositional system, central High Atlas rift basin, Morocco.
1286 Sedimentology 55, 773–807. https://doi.org/10.1111/j.1365-3091.2007.00921.x
1287 Winter, A., Jordan, R.W., Roth, P.H., 1994. Biogeography of living coccolithophores in
1288 ocean waters. In: Winter, A., Siesser, W. (Eds.), Coccolithophores. Cambridge
1289 University Press, Cambridge, pp. 161–177.
1290 Young, J.R., 1994. Functions of coccoliths. In: Winter, A., Siesser, W. (Eds.),
1291 Coccolithophores. Cambridge University Press, pp. 63–82.
1292
1293 Supplementary Material.

Figure A. X-ray diagrams of the clay fraction of samples from the Mellala section (MLL) and from Raknet El-Khala (RK). All values are expressed as d-spacings. I=illite; C+CV=mixture of chlorite and chlorite-vermiculite mixed-layer; IS=illite-smectite R1-R3 type mixed-layer; Q=quartz.

The clay mineral assemblages in the two sections, Mellala and Raknet El-Kahla, consist mainly of a mixture of relatively well-crystallized illite (main $d_{(00l)}$ peaks at 10, 5 and 3.33 Å) and chlorite (main $d_{(00l)}$ peaks at 14.2, 7.1, 4.72, 3.53 Å; Fig. A). Small proportions of undistinguishable R1 and R3 type illite-smectite mixed-layers (R1-R3 IS) indicated by peaks close to those of illite are also recognized and are responsible for the asymmetry of the 10 Å peak (Fig. A). The enlargement and the displacement to lower values of the 14.1 and 3.53 Å peaks within the heating treatment likely indicate that chlorite is mixed with vermiculite, so that true chlorite and chlorite-vermiculite may coexist in the assemblage. No trace of smectite, R0 type IS mixed-layer or kaolinite was evidenced by XRD analyses.

The most prominent feature of the clay assemblage of the Mellala and Raknet El-Kahla sections is the absence of kaolinite, although this mineral is common in the uppermost Pliensbachian and Toarcian sediments from the Tethys domain (Dera et al., 2009; Hermoso and Pellenard 2014; Bougeault et al., 2017; Deconinck et al., 2019). This absence can either be attributed to arid or semi-arid climate conditions, preventing the formation of kaolinite during pedogenesis, or can be related to the disappearance of kaolinite by illitization processes during burial diagenesis, as generally observed for burial temperatures higher than 120°C (Chamley et al., 1989; Lanson et al., 2002). The absence of smectite and R0 type IS mixed-layer clay minerals is expected, as these latter are more sensitive to burial diagenesis and illitization processes. However, under arid climates they should have been formed abundantly in soils introduced from adjacent areas. Here, it is not possible to definitively discriminate between diagenetic and climatic processes, as significant burial diagenesis occurred thus preventing the use of clay mineral assemblages for climate and palaeoenvironment interpretations. However, clay mineralogy data are coherent with the poor preservation of calcareous nannofossils that can be explained by a strong burial diagenesis, as also reported for the High-Altas of Morocco (Dera et al., 2009; Mercuzot et al., 2019). The overall conditions at Mellala and

Raknet El-Kahla, which were located at low latitudes and characterized by an arid climate during the end Pliensbachian and Toarcian, however, were unfavourable for kaolinite formation, as it was also suggested for the Asturian Basin (North Spain; Deconinck et al., 2020).

Supplementary references

Bougeault, C., Pellenard, P., Deconinck, J.F., Hesselbo, S.P., Dommergues, J.L., Bruneau, L., Cocquerez, T., Laffont, R., Huret, E., Thibault, N.R., 2017. Climatic and palaeoceanographic changes during the Pliensbachian (Early Jurassic) inferred from clay mineralogy and stable isotope (CO) geochemistry (NW Europe). Global and Planetary Change 149, 139–152.

Chamley, H., 1989. Clay Sedimentology. Springer Verlag, 623 pp.

Deconinck, J.F., Hesselbo, S.P., Pellenard, P., 2019. Climatic and sea-level control of Jurassic (Pliensbachian) clay mineral sedimentation in the Cardigan Bay Basin, Llanbedr (Mochras Farm) borehole Wales. Sedimentology 66, 2769–2783.

Deconinck, J.F. Gómez, J.J., Baudin, F., Biscay, H., Bruneau, L., Cocquerez, T., Mathieu, O., Pellenard, P., Santoni, A.L., 2020. Diagenetic and environmental control of the clay mineralogy, organic matter and stable isotopes (C, O) of Jurassic (Pliensbachian-Lowermost Toarcian) sediments of the Rodiles section (Asturian Basin, Northern Spain). Marine and Petroleum Geology, 115, 104286, https://doi.org/10.1016/j.marpetgeo.2020.104286

Dera, G., Pellenard, P., Neige, P., Deconinck, J.-F., Pucéat, E., Dommergues, J.-L., 2009b. Distribution of clay minerals in Early Jurassic Peritethyan seas: Palaeoclimatic significance inferred from multiproxy comparisons. Palaeogeography, Palaeoclimatology, Palaeoecology 271, 39–51.

Hermoso, M., Pellenard, P., 2014. Continental weathering and climatic changes inferred from clay mineralogy and paired carbon isotopes across the early to middle Toarcian in the Paris Basin. Palaeogeography, Palaeoclimatology, Palaeoecology 399, 385-393.

Lanson, B., Beaufort, D., Berger, G., Bauer, A., Cassagnabere, A., Meunier, A., 2002. Authigenic kaolin and illitic minerals during burial diagenesis of sandstones: a review. Clay minerals 37, 1-22.

Mercuzot, M., Pellenard, P., Durlet, C., Bougeault, C., Meister, C., Dommergues, J.L., Thibault, N., Baudin, F., Mathieu, O., Bruneau, L., Huret, E., El Mhidi, K., 2019. Carbon-isotope events during the Pliensbachian (Lower Jurassic) on the African and European margins of the NW Tethyan Realm. Newsletters on Stratigraphy. Published online 10.1127/nos/2019/0502

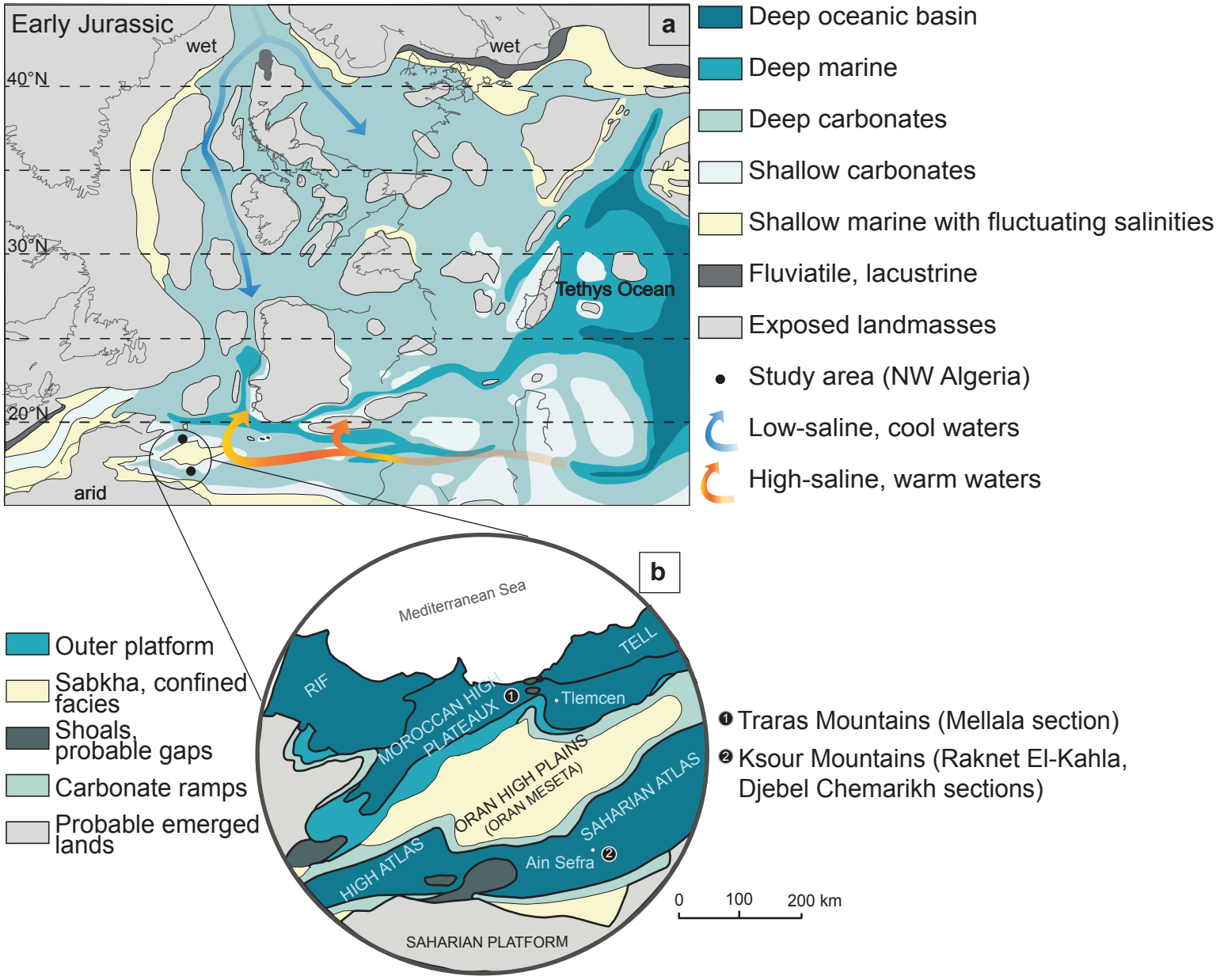

Figure 1 (Baghli et al.)

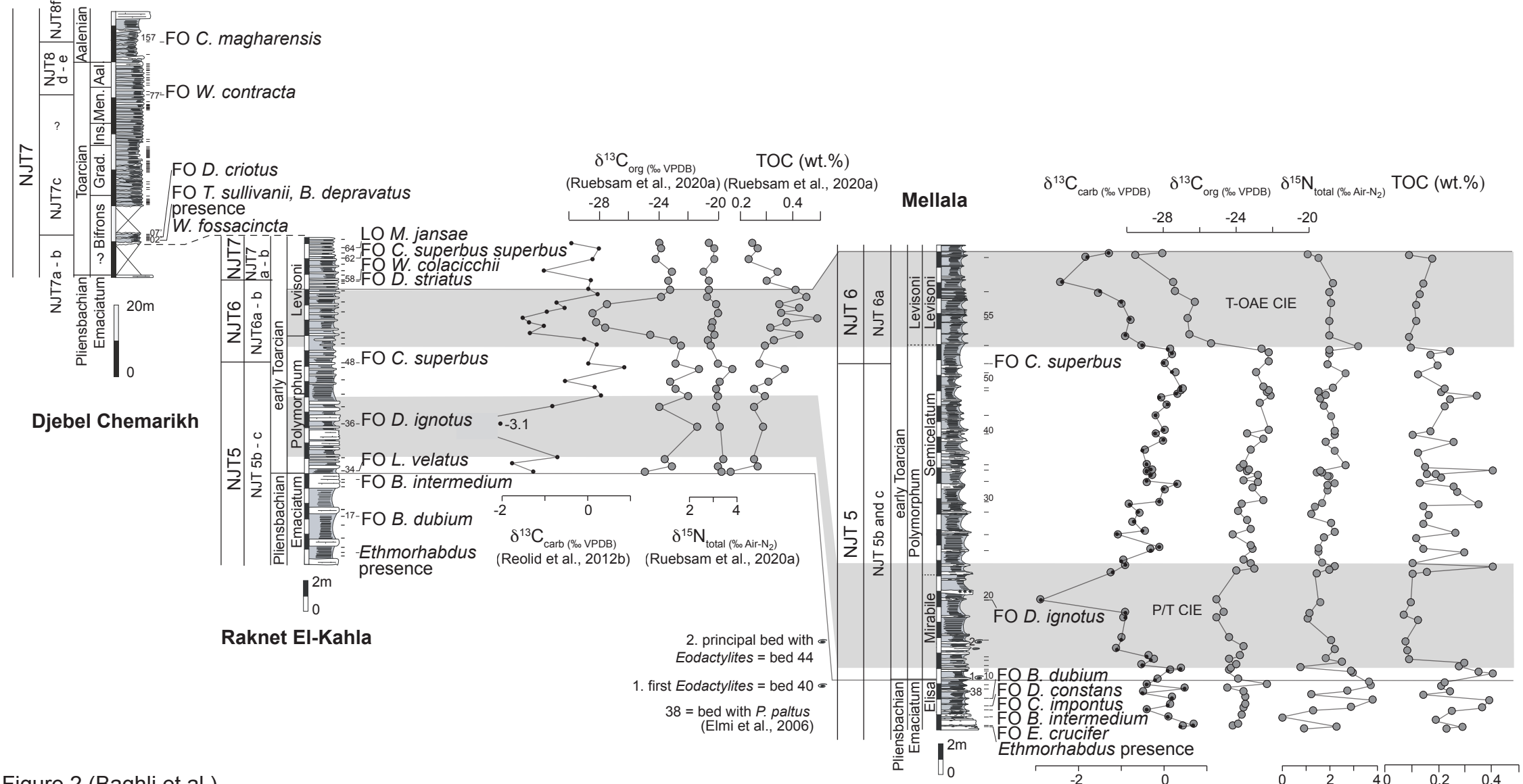

Figure 2 (Baghli et al.)

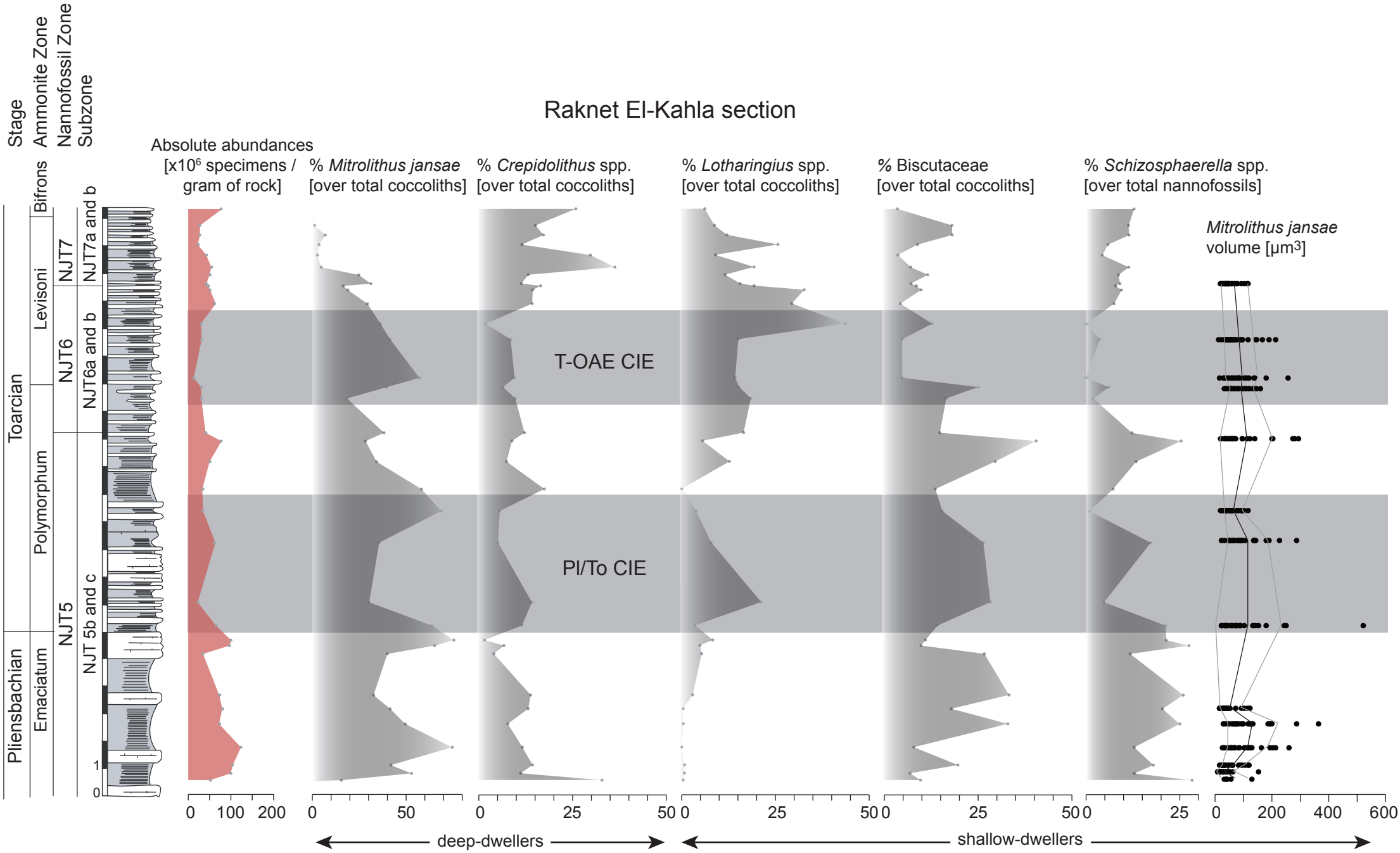

Figure 3 (Baghli et al.)

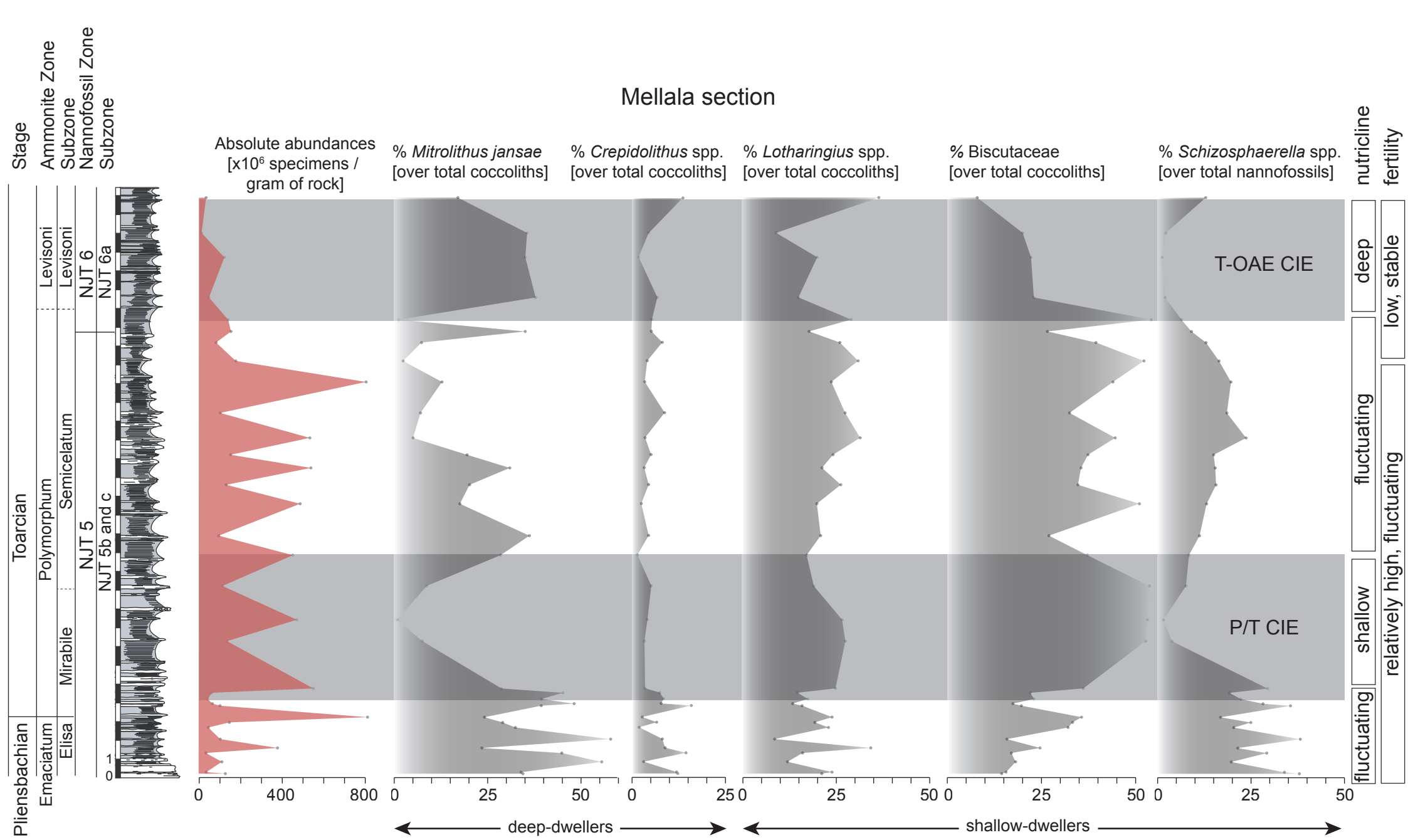

Figure 4 (Baghli et al.)

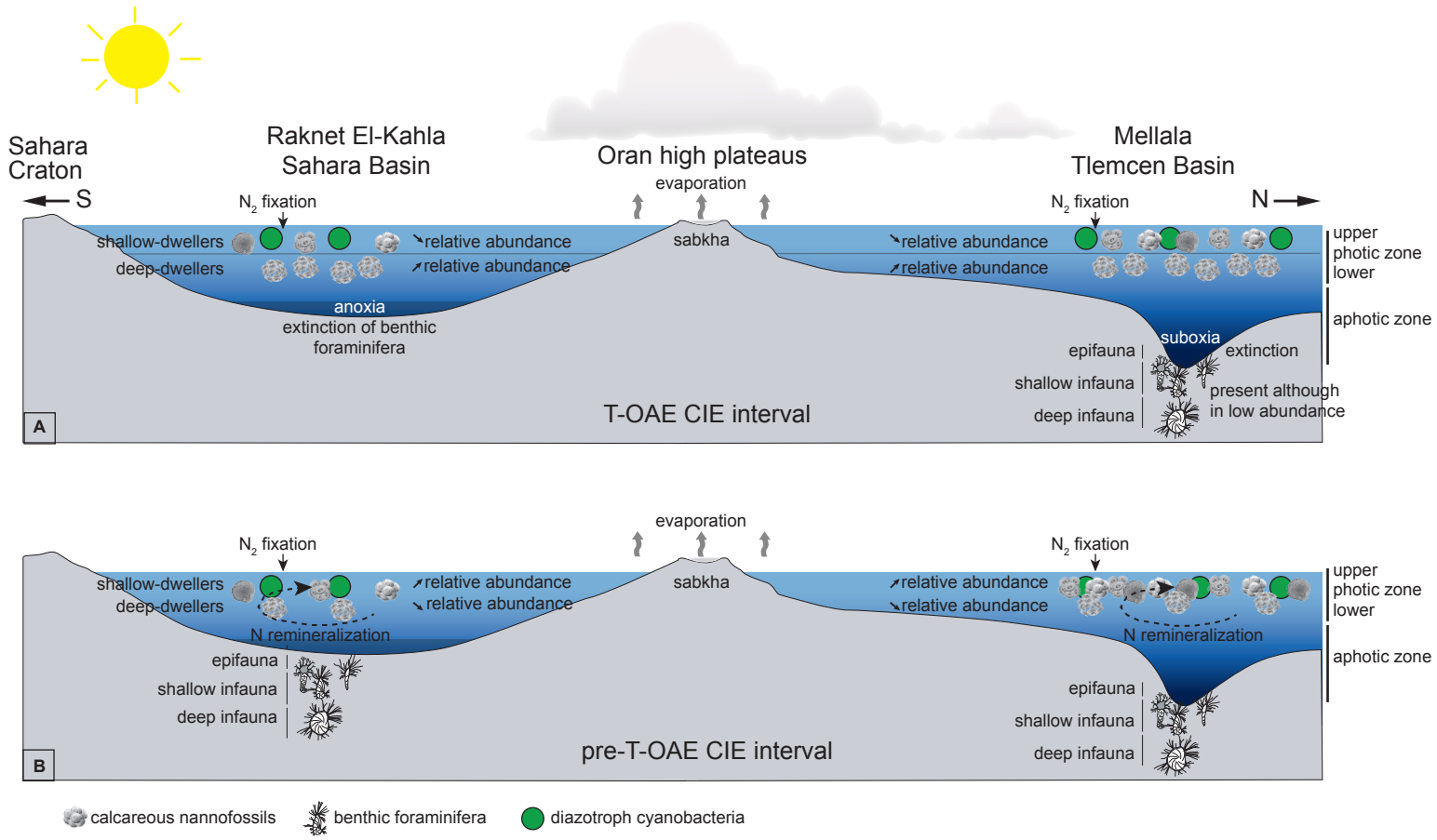

Figure 5 (Baghli et al.)

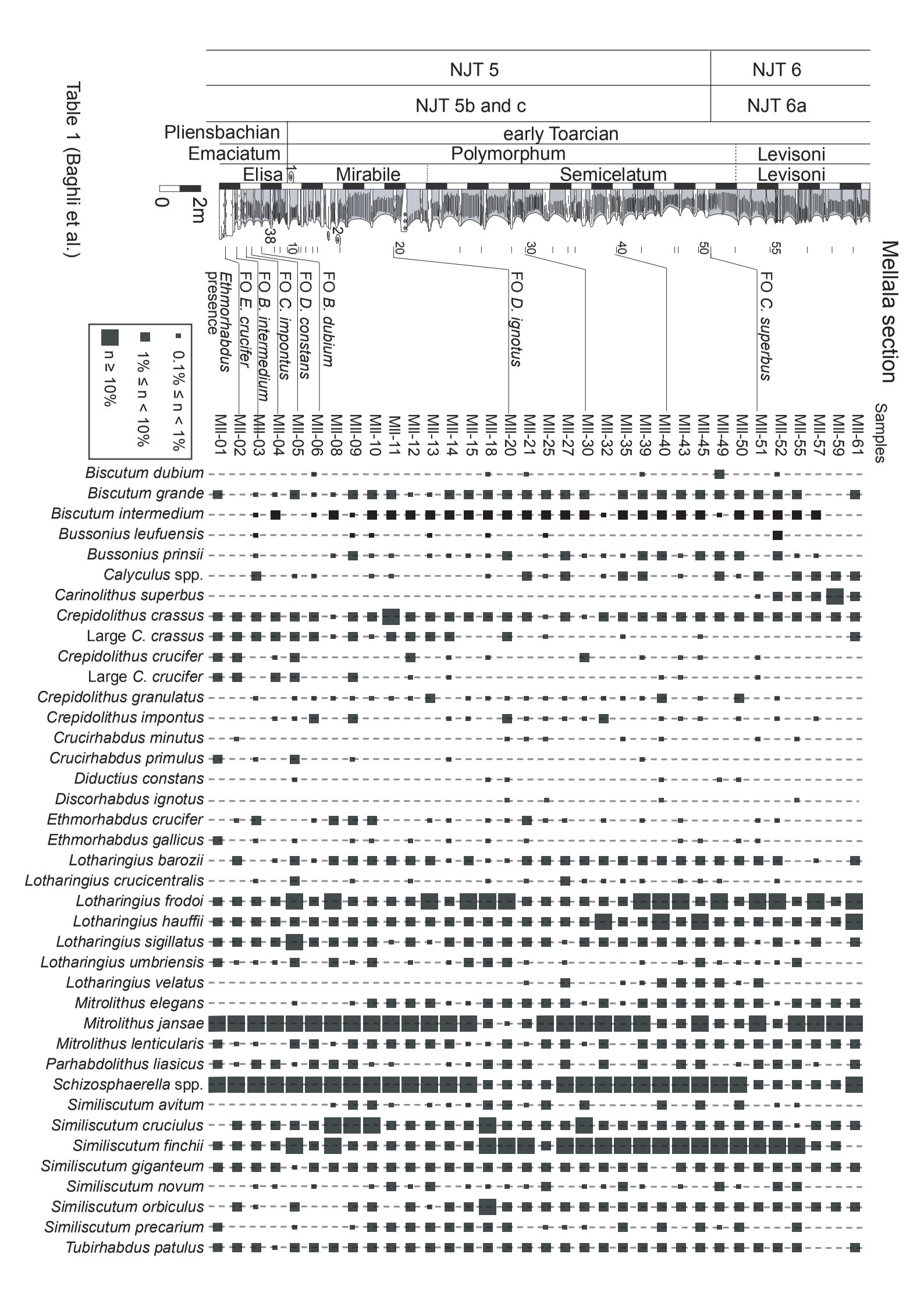
Table 1 (Baghli et al.)
NJT 5
NJT 6
NJT 5b and c
NJT 6a
Pliensbachian
early Toarcian
Emaciatum
Polymorphum
Levisoni
Elisa
Mirabile
Semicelatum
Levisoni
0
2m
Ethmorhabdus presence
FO E. crucifer
FO B. intermedium
FO C. impontus
FO D. constans
FO B. dubium
FO D. ignotus
FO C. superbus
n ≥ 10%
1% ≤ n < 10%
0.1% ≤ n < 1%
Mellala section
Samples
MII-01
MII-02
MII-03
MII-04
MII-05
MII-06
MII-08
MII-09
MII-10
MII-11
MII-12
MII-13
MII-14
MII-15
MII-18
MII-20
MII-21
MII-25
MII-27
MII-30
MII-32
MII-35
MII-39
MII-40
MII-43
MII-45
MII-49
MII-50
MII-51
MII-52
MII-55
MII-57
MII-59
MII-61
Biscutum dubium
Biscutum grande
Biscutum intermedium
Bussonius leufuensis
Bussonius prinsii
Calyculus spp.
Carinolithus superbus
Crepidolithus crassus
Large C. crassus
Crepidolithus crucifer
Large C. crucifer
Crepidolithus granulatus
Crepidolithus impontus
Crucirhabdus minutus
Crucirhabdus primulus
Diductius constans
Discorhabdus ignotus
Ethmorhabdus crucifer
Ethmorhabdus gallicus
Lotharingius barozii
Lotharingius crucicentralis
Lotharingius frodoi
Lotharingius hauffii
Lotharingius sigillatus
Lotharingius umbriensis
Lotharingius velatus
Mitrolithus elegans
Mitrolithus jansae
Mitrolithus lenticularis
Parhabdolithus liasicus
Schizosphaerella spp.
Similiscutum avitum
Similiscutum cruciulus
Similiscutum finchii
Similiscutum giganteum
Similiscutum novum
Similiscutum orbiculus
Similiscutum precarium
Tubirhabdus patulus


NJT5
NJT6
NJT7
NJT 5b - c
NJT6a - b
NJT7 a - b
Pliensbachian
early Toarcian
Emaciatum
Polymorphum
Levisoni
Raknet El-Kahla section
17 – FO B. dubium
34 – FO L. velatus
– FO B. intermedium
36
FO D. ignotus
48
FO C. superbus
58
FO D. striatus
FO W. colacicchii
62
FO C. superbus
64 – LO M. jansae
– Ethmorhabdus presence
n ≥ 10%
1% ≤ n < 10%
0.1% ≤ n < 1%
Samples
RK 01 NM
RK 02 NM
RK 03 NM
RK 06 NM
RK 14 NM
RK 17 NM
RK 20 NM
RK 29 NM
RK 30 NM
RK 31 NM
RK 34 NM
RK 35 NM
RK 36' NM
RK 39 NM
RK 41 NM
RK 42 NM
RK 47 NM
RK 48 NM
RK 50 NM
RK 51 NM
RK 51'NM
RK 52 NM
RK 53 NM
RK 55 NM
RK 56 NM
RK 57 NM
RK 58 NM
RK 59 NM
RK 60 NM
RK 61 NM
RK 62 NM
RK 63 NM
RK 64' NM
RK 65 NM
Biscutum dubium
Biscutum grande
Biscutum intermedium
Calyculus spp.
Large Calyculus spp.
Carinolithus poulnabronei
Carinolithus superbus
C. superbus superbus
Crepidolithus crassus
Large C. crassus
Crepidolithus crucifer
Large C. crucifer
Crepidolithus granulatus
Discorhabdus ignotus
Discorhabdus striatus
Ethmorhabdus crucifer
Lotharingius barozii
Lotharingius crucicentralis
Lotharingius frodoi
Lotharingius hauffii
Lotharingius sigillatus
Lotharingius umbriensis
Lotharingius velatus
Mitrolithus elegans
Mitrolithus jansae
Mitrolithus lenticularis
Parhabdolithus liasicus
P. liasicus distinctus
Schizosphaerella spp.
Similiscutum avitum
Similiscutum cruciulus
Similiscutum finchii
Large S. finchii
Similiscutum giganteum
Similiscutum novum
Similiscutum orbiculus
Similiscutum precarium
Tubirhabdus patulus
Tubirhabdus sp.
W. fossacincta

Djebel Chemarikh section

Samples

20m

0

NJT8f

NJT8d - e

?

NJT7c

NJT7a - b

Aalenian

Toarcian

Pliensbachian

Aalensis

Meneghinii

Insigne.

Gradata

Bifrons

Emaciatum

?

157

77'

20

10'

FO *C. magharensis*

FO *W. contracta*

FO *D. criotus*

FO *T. sullivanii, B. depravatus*
presence *W. fossacincta*

0.1% ≤ n < 1%

1% ≤ n < 10%

n ≥ 10%

157
132'
129'
128'
112'
111'
103'
102
101'
99'
98'
96'
95'
87'
78'
77'
76'
74'
73'
67'
63'
60
58
57'
56'
56
55
54
53
52
51'
51
50
49'
49
48
44
43
42
41'
40
39
38
35
34
33
32'
32
30
29'
29
27
26'
26
24
23
22
21
20
19
18
17
16
15'
14
14'
13'
12
10'
08'
07'
07
06'
05'
04'
03'
02'
01'

Schizosphaerella
B. dubium
B. finchii
B. novum
B. grande
B. depravatus
B. intermedium
B. leufuensis
B. prinsii
Calyculus
C. cavus
C. crassus
C. granulatus
C. cantaluppi
C. poulnabronei
C. superbus
D. ignotus
D. striatus
D.criotus
D. constans
C. magharensis
L. barozii
L. crucicentralis
L. aff. L. crucicentralis
L. frodoi
L. hauffii
L. sigillatus
L. umbriensis
L. velatus
Mazaganella
M. elegans
M. lenticularis
P. liasicus
R. incompta
S. novum
T. sullivanii
T. patulus
W. colacicchii
W. contracta
W. fossacincta